

1           **Aerosol immission maps and trends over Germany with hourly data at four rural**  
2                               **background stations from 2009 to 2018**

3  
4 Jost Heintzenberg<sup>1</sup>, Wolfram Birmili<sup>2</sup>, Bryan Hellack<sup>2</sup>, Gerald Spindler<sup>1</sup>, Thomas Tuch<sup>1</sup>, and  
5 Alfred Wiedensohler<sup>1</sup>

6 1: Leibniz Institute for Tropospheric Research (TROPOS), Permoserstr. 15, 04318 Leipzig,  
7 Germany

8 2: German Environment Agency, Wörlitzer Platz 1, 06844 Dessau-Roßlau, Germany

9  
10  
11 **Abstract**

12 Ten years of hourly aerosol and gas data at four rural German stations have been combined  
13 with hourly back trajectories to the stations and inventories of the European EDGAR emission  
14 database yielding immission maps over Germany of PM<sub>10</sub>, particle number concentrations, and  
15 equivalent black carbon (eBC). The maps reflect aerosol emissions modified with atmospheric  
16 processes during transport between sources and receptor sites. Compared to emission maps  
17 strong Western European emission centers do not dominate the downwind concentrations  
18 because their emissions are reduced by atmospheric processes on the way to the receptor area.  
19 PM<sub>10</sub>, eBC, and to some extent also particle number concentrations are rather controlled by  
20 emissions from Southeastern Europe from which pollution transport often occurs under dryer  
21 conditions. Newly formed particles are found in air masses from a broad sector reaching from  
22 Southern Germany to Western Europe which we explain with gaseous particle precursors  
23 coming with little wet scavenging from this region.

24 Annual emissions for 2009 of PM<sub>10</sub>, BC, SO<sub>2</sub>, and NO<sub>x</sub> were accumulated along each  
25 trajectory and compared with the corresponding measured time series. The agreement of each  
26 pair of time series was optimized by varying monthly factors and annual factors on the 2009

27 emissions. This approach yielded broader summer emission minima than published values that  
28 were partly displaced from the midsummer positions. The validity of connecting immission  
29 and emission of particulate pollution was tested by calculating temporal changes of eBC for  
30 subsets of back trajectories passing over two separate prominent emission regions, region A to  
31 the Northwest and B to the Southeast of the measuring stations. Consistent with reported  
32 emission data the calculated immission decreases over region A are significantly stronger than  
33 over region B.

34

35

## 36 **1 Introduction**

37

38 The atmospheric aerosol is known to influence the Earth's radiation budget because it directly  
39 scatters and absorbs solar radiation (Schwartz, 1996; Bond et al., 2013), and acts as cloud  
40 condensation nuclei, thus modulating the optical properties and lifetimes of clouds (Twomey,  
41 1974; Penner et al., 2004). In many regions of the globe that had undergone industrialization  
42 early on, anthropogenic aerosol concentrations are currently in decline (Leibensperger et al.,  
43 2012; Zanatta et al., 2016). With respect to declining concentrations and emissions, Samset al.  
44 (2018) suggest that removing present-day anthropogenic aerosol emissions – assuming constant  
45 greenhouse gas emissions, could lead to a global mean surface heating as high as 0.5–1.1°C.

46

47 Besides climate, the atmospheric aerosol has been acknowledged to influence human health  
48 through respiratory and cardiovascular health endpoints (Anderson et al., 2012). Lelieveld et  
49 al., (2015) quantified the world-wide burden of disease (premature mortality) due to outdoor  
50 pollution, large part of which was attributed to airborne particulate matter. It is apparent that  
51 the distribution of adverse health effects is very uneven among the world-wide population,  
52 depending on the local level of outdoor pollution.

53

54 In view of the described man-driven effects it seems imperative to develop instruments to  
55 reliably monitor changes in anthropogenic aerosol concentrations as well as an understanding  
56 of the balance between aerosol sources and measured concentrations. Researchers have strived  
57 to obtain a spatial picture of the distribution of pollutants, and to achieve a connection between  
58 the sources of pollution and concentrations downwind. A widely used method has been the  
59 extrapolation of concentrations measured in one or several locations into two-dimensional  
60 space through the use of meteorological dispersion approaches: The first maps of particulate

61 air pollutants over Europe were constructed in the 1970s with the help of coarse emission data  
62 and simple trajectory models (Eliassen, 1978). Statistical methods were developed to connect  
63 pollution sources and ensuing aerosol concentrations at receptor sites (Miller et al., 1972;  
64 Friedlander, 1973; Cass and McRae, 1983). By combining statistics with back trajectory data  
65 sectorial information about sources controlling the composition of the aerosol over Southern  
66 Sweden was derived by Swietlicki et al., (1988). Later the approach of using back trajectories  
67 to map aerosol sources was refined by Stohl (1996) and tested with one-year sulfate data from  
68 the co-operative program for monitoring and evaluation of the long-range transmission of air  
69 pollutants in Europe (EMEP, [www.emep.int](http://www.emep.int)). In a similar approach with five years of aerosol  
70 data from a single Siberian receptor site Heintzenberg et al. (2013) identified potential source  
71 regions over Eurasia and with aerosol data from four Swedish icebreaker expeditions over the  
72 Central Arctic (Heintzenberg et al., 2015). Charron et al. (2008) constructed concentration field  
73 maps to identify the source regions of specific types of aerosol particle size distributions  
74 arriving in England. All these works share the approach that time-dependent information on  
75 concentrations measured at receptor site(s) are transformed into space, thus allowing  
76 conclusions on the potential source regions of gaseous and/or particulate emissions.

77

78 With more comprehensive air quality models concentrations of specific aerosol were  
79 mapped over Europe together with short temporal developments (e.g., Schell et al., 2001). For  
80 specific episodes high spatial resolution aerosol concentration maps in urban and non-urban  
81 European areas have been generated with sophisticated chemistry transport models (e.g.,  
82 Beekmann et al., 2015; Riemer et al., 2004; Wolke et al., 2004). For the years 2002 and 2003  
83 Marmer and Langman (2007) analyzed the spatial and temporal variability of the aerosol  
84 distribution over Europe with a regional atmosphere-chemistry model. They found that  
85 meteorological conditions play a major role in spatial and temporal variability in the European  
86 aerosol burden distribution. Regionally, year to year variability of modeled monthly mean

87 aerosol burden reached up to 100% because of different weather conditions.

88

89 In the present study ten years of hourly aerosol data at four German stations were available  
90 for the identification of potential source regions. As it appears unrealistic to analyze such a  
91 large database with advanced chemical transport models we resorted to the well proven  
92 approach of utilizing back trajectories cited above and connected the results to emission fields.  
93 We define the resulting concentration maps of particulate and gas parameters as immission  
94 maps because they represent long-term average emissions of air pollutants modified by the  
95 controlling atmospheric processes along the pathways to the receptor sites. In Charron et al.  
96 (2008) this approach is termed “concentration field map method”. With a much larger data set  
97 spanning a much tighter network of 1500 stations Rohde and Muller (2015) used the Kriging  
98 interpolation approach (Krige, 1951) to construct air pollution maps over China. Another  
99 approach to construct pollution maps over the province Henan, China was used by Liu et al.,  
100 (2018). They combined an emission inventory with chemical modeling and back trajectories  
101 to derive high resolution maps of particulate and gaseous pollution components and find that  
102 emissions from neighboring provinces are important contributors to local air pollution levels.

103

104 Recent political, economic and technological developments in Europe have caused  
105 substantial changes in the emission of air pollutants. Lavanchy et al. (1999) deduced a trend in  
106 atmospheric black carbon from preindustrial times to 1975. Strong downward trends in major  
107 aerosol components before and after the German reunification (1983-1998) over rural East  
108 Germany were reported by Spindler et al., (1999). For the years 2003 – 2009 Kuenen et al.,  
109 (2014) published trends in the development of aerosol emissions as elaborated from reported  
110 emissions. The German Environmental Agency (GEA) publishes trends in air pollution as  
111 measured at a number of ca. 380 federal and state air quality stations (Minkos, 2019).

112 According to these records, PM<sub>10</sub> mass concentrations declined by approximately 25 % over  
113 the period 2000-2019

114

115 Combining long-term aerosol and gas data at the four stations of the present study provide  
116 an excellent data base for identifying both the most important source regions and possible  
117 temporal changes. During the ten recent years covered by our data we expected noticeable  
118 systematic changes in our time series that can be interpreted in terms of emissions. As a side  
119 result in the process of deriving long-term emission trends of major air pollutants over Germany  
120 information of the monthly disaggregation of annual aerosol emissions can be derived.

121

122

## 123 **2 Aerosol and trace gas data**

124

125 The core data of the present study have been measured at the stations Melpitz (ME),  
126 Neuglobsow (NG), and Waldhof (WA) of the German Ultrafine Aerosol Network GUAN  
127 network (Birmili et al., 2016) and at station Collmberg (CO) operated by the Saxonian  
128 Environment Agency. These four rural background stations lie in the northeastern lowlands of  
129 Germany at distances between 30 and 205 km from each other. Ten-year-average particle mass  
130 concentrations under 10 µm particle diameter (PM<sub>10</sub>) and their standard deviations at the four  
131 stations are rather similar: 15±13, 22±12, 14±10, and 15±11 µgm<sup>-3</sup> at CO, ME, NG, and WA,  
132 respectively. The corresponding long-term average particle number concentrations between 10  
133 and 800 nm particle diameter (N<sub>10-800</sub>) and their standard deviations at the three GUAN-stations  
134 are 5400±4100, 3600±2300, and 4300±2800 cm<sup>-3</sup>, respectively. Basic statistics on particle  
135 number and eBC mass concentrations of the three GUAN-stations were presented in Sun et al.  
136 (2019) whereas details about instrumentation and their maintenance can be found in Birmili et

137 al., (2016). The ensemble of hourly data at the four stations is the base of the pollution maps  
138 derived in this work.

139

140 TROPOS-type mobility particle size spectrometers (MPSS, Wiedensohler et al., 2012) were  
141 used to record particle number size distributions across the particle size range 10-800 nm.  
142 Quality assurance of the long-term measurements followed the recommendations of  
143 Wiedensohler et al. (2018) including weekly inspections as well as monthly and annual  
144 maintenance intervals. Once a year the MPSS were intercompared against a reference MPSS  
145 of the WCCAP (World Calibration Center for Aerosol Physics) either on-site and/or at the  
146 calibration facility. The lower detection limit of the MPSS is around  $30 \text{ cm}^{-3}$  for a time  
147 resolution of 30 minutes. Equivalent Black Carbon (eBC) was determined by multi-angle  
148 absorption photometers (MAAP) using a mass absorption cross section of  $6.6 \text{ m}^2 \text{ g}^{-1}$  (Petzold  
149 et al., 2013; Nordmann et al., 2013; Birmili et al., 2016). An intercomparison of multiple  
150 MAAP instruments resulted in an inter-device variability of less than 5% (Müller et al., 2011).  
151 While the MAAP deployed at the TROPOS station Melpitz was biannually compared to the  
152 reference absorption photometer at the WCCAP in Leipzig, the instruments at the UBA stations  
153 Waldhof and Neuglobsow were serviced by the manufacturer. For hourly measurements of  
154  $\text{PM}_{10}$  continuous oscillating microbalances (Thermo Scientific TEOM 1400) were utilized at  
155 stations CO, NG, and WA. At station ME  $\text{PM}_{10}$  was determined in daily filter samples (0:00  
156 to 24:00 CET), Spindler et al. (2013). The TEOM1400-instrument and gravimetric filter  
157 sampling are different methods for particle mass concentrations. The TEOM collects  
158 particulate mass on a vibrating substrate (tapered element) and registers the change of the  
159 oscillation frequency that is decreasing with mass loading (Patashnick and Rupprecht, 1991).  
160 The TEOM operates at a constant temperature setting above ambient (typically 30– 50°C) to  
161 prevent contraction and expansion of the tapered element and reduce interferences from water  
162 vapor condensation. However, heating the ambient air enhances volatilization of particle-

163 bound semivolatile compounds (e.g., ammonium nitrate and some organic species) resulting in  
164 an underestimation of PM when semivolatile material dominates the particulate phase during  
165 cold seasons. The condensation and evaporation of ammonium nitrate and organic species can  
166 also influence the filter sampling under ambient conditions. Here the effect can be balanced  
167 partly by the temperature variation during the daily filter sampling. However, the results of both  
168 methods mostly are in good agreement (e.g., Zhu et al., 2007).

169

170 Hourly aerosol data from the three GUAN-stations during 2009 – 2015 (NG  $\geq$ 2011) have  
171 been utilized in a previous study (Heintzenberg et al., 2018) to understand aerosol processes  
172 during air mass transport between the stations. In the present study the data set was enlarged  
173 to include the additional station Collmberg and data at all stations from the year 2016 through  
174 2018. The integral aerosol parameters particle number concentration ( $N_{10-800}$ ,  $\text{cm}^{-3}$ ), light  
175 absorption-equivalent mass concentration of Black Carbon (eBC,  $\mu\text{g m}^{-3}$ ), and particle mass  
176 concentrations under 10  $\mu\text{m}$  particle diameter ( $\text{PM}_{10}$ ,  $\mu\text{g m}^{-3}$ ) were utilized.  $N_{10-800}$  is based on  
177 the integral over measured particle size distributions from 10 to 800 nm.

178

179  $\text{NO}_x$  and  $\text{SO}_2$  emitted by anthropogenic combustion processes are transformed in the  
180 atmosphere and add to the anthropogenic aerosol. At the three GUAN stations both are  
181 measured with the same temporal resolutions as the aerosol data. Additionally, at Collmberg  
182  $\text{NO}_x$ -data could be utilized in the interpretation of the aerosol data. The trace gas analyzers for  
183  $\text{NO}_x$  and  $\text{SO}_2$  were calibrated with test gases for NO (NO in  $\text{N}_2$ ) and  $\text{SO}_2$  ( $\text{SO}_2$  in  $\text{N}_2$ , both Air  
184 Liquide, Germany).  $\text{NO}_2$  was produced in a gas phase titration device (GPT APMC370,  
185 Horiba, Germany) by quantitative oxidation of NO test gas (Rehme, 1976). The trace gas  
186 analyzers were used in an optimal range and all registered values (also below the detection  
187 limit) were used for this long-term study. As most particle numbers in polluted continental  
188 environments tropospheric ozone is a secondary atmospheric pollutant. We utilized hourly



189 ozone data taken at all four stations throughout the studied time period as ancillary information  
190 in the discussion of particle-number related results. For the ozone measurements a common  
191 trace gas ozone monitor was used (Horiba APOA-350). This device quantifies tropospheric  
192 ozone by UV Absorption and use the cross-flow modulation principle. Ambient air with and  
193 without ozone (elimination by a selective scrubber) was used alternatively in the measuring  
194 cuvette yielding a very stable ozone signal. The devices were calibrated using an ozone-  
195 standard (Ozon-Calibrator, Thermo Environmental Instruments 49PS).

196

197 Table 1 gives an overview over the instrumental characteristics of all stations and the total  
198 number of validated data hours for each utilized component. The minimum is 57962 hours for  
199 validated MPSS-data at the three GUAN-stations and the maximum with 88838 validated data  
200 hours for NO<sub>x</sub> at all four stations. Strictly concurrent (by the hour) are less validated data hours.  
201 For MPSS, eBC, and SO<sub>2</sub>-data at the GUAN-stations this numbers is 48533 hours, and 48114  
202 and 47729 hours for PM<sub>10</sub> and NO<sub>x</sub>-data, respectively, at all four stations. However, these  
203 reduced strictly concurrent numbers do not substantially affect the 10-year-average maps  
204 discussed below.

205

206

### 207 **3 Back trajectories**

208

209 With the HYSPLIT4 model (Stein et al., 2015) and based on the meteorological fields from the  
210 Global Data Assimilation System with one-degree resolution (GDAS1,  
211 <https://www.emc.ncep.noaa.gov/gmb/gdas/>) three-dimensional trajectories were calculated  
212 arriving every hour at a height of 500m above ground level at the four stations. The trajectories  
213 were calculated backward for up to five days using the meteorological fields from the server at

214 Air Resources Laboratory (ARL), NOAA (<http://ready.arl.noaa.gov>), where more information  
215 about the GDAS dataset can be found. Turbulent atmospheric mixing is included in  
216 parameterized form in HYSPLIT4. The present study utilizes the default version of this  
217 parameterization according to Draxler and Hess (1998). The back trajectories are calculated  
218 with the base version of HYSPLIT4 that does not include any specific dispersion and  
219 scavenging of atmospheric trace substances. Precipitation along the trajectories was used in  
220 the interpretation of the immission maps. The precipitation values mapped in the present study  
221 and the temperature values used in the trend discussion of  $N_{10-800}$  are those listed by HYSPLIT4  
222 at each point of a trajectory. They are meteorological parameters at the nearest grid cell of the  
223 assimilated global meteorological fields provided by the U.S. National Weather Service's  
224 National Centers for Environmental Prediction (NCEP) (Kanamitsu, 1989). Average  
225 horizontal wind speeds in between two one-hour trajectory steps were calculated from the  
226 distance covered by a trajectory between two successive steps. With the 350593 hourly back  
227 trajectories from the four stations the time series of  $N_{10-800}$ ,  $PM_{10}$ , and eBC were extrapolated  
228 over Germany and part of the neighbor countries. At Melpitz  $PM_{10}$ -data were only available  
229 as daily averages. Thus, the daily average concentrations were extrapolated along each hourly  
230 trajectory of the respective day.

231

232

#### 233 **4 Emission data**

234

235 For the interpretation of the immission maps we used the emission data set version 4.3.2 for  
236 2009 of the components particle mass concentrations below  $10\ \mu\text{m}$  ( $PM_{10}$ ), BC,  $NO_x$  and  $SO_2$   
237 as compiled in the Emissions Data Base for Global Atmospheric Research (EDGAR,  
238 [https://edgar.jrc.ec.europa.eu/overview.php?v=432\\_AP](https://edgar.jrc.ec.europa.eu/overview.php?v=432_AP), DOI (<https://data.europa.eu/doi/10.29>

239 04/JRC\_DATASET\_EDGAR). This data set concerns primary emissions only and has been  
240 introduced by Crippa et al., (2018). All human activities, except large scale biomass burning  
241 and land use, land-use change, and forestry are included in the data base. Emissions of coarse  
242 particles from agricultural surfaces are not included. They are, in fact, very sensitive to soil  
243 and weather conditions, and thus not trivial to quantify. Primary aerosol emission data are  
244 generally characterized by rather high uncertainties. For the EDGAR data base Crippa et al.  
245 (2018) report a range of variation in 2012 between 57.4% and 109.1% for PM<sub>10</sub>, and between  
246 46.8% and 92% for BC. Even higher uncertainties in PM emissions might come from super-  
247 emitting vehicles that are not considered in this data base (Klimont et al., 2017). In our maps  
248 and trend calculations we applied the grid values of emission data that were listed in the  
249 EDGAR inventories no more than 30 km away from any trajectory time step.

250

251

## 252 **5 Results and discussion**

### 253 **5.1 Aerosol concentration maps (immission maps)**

254 The trajectory-extrapolated N<sub>10-800</sub>, PM<sub>10</sub>, and eBC from the four stations yielded immission  
255 maps averaged over the period 2009 – 2018, that are collected in Figs. 1-2. Both, the particle-  
256 number related N<sub>10-800</sub> and the particle-mass related PM<sub>10</sub>, and eBC exhibit systematic seasonal  
257 variations. Most events of new particle formation (NPF) over the continents occur during the  
258 photochemically active summer months (Kulmala et al., 2004) whereas the particle-mass  
259 related aerosol parameters due to combustion processes exhibit highest concentrations during  
260 the winter months (Matthias et al., 2018). Consequently, we constructed two maps for each  
261 discussed component: One of averages over the months April through October and one of  
262 averages over the months November through March. Only map cells with at least 300 trajectory  
263 hits are discussed. Interpreting these hits in terms of Poisson-statistics would then yield a

264 maximum uncertainty of 5.8% per cell. In terms of a Gaussian statistic the arithmetic cell-  
265 averages displayed in the maps exhibit standard deviations of cell averages that are less than  
266 six percent.

267

268 The maps of  $N_{10-800}$  in Fig. 1 show distributions of air masses over Germany and adjacent  
269 countries related to particle numbers instead of particulate mass. There are two arguments for  
270 showing maps of number related results. First, particle number concentrations are connected  
271 with cloud processes, their formation (Pruppacher and Klett, 1978), radiative effects, e.g.,  
272 albedo (Twomey, 1974), and precipitation (Li et al., 2011). Second, in the area of aerosol-  
273 health issues ultrafine particles (< 100 nm diameter) have been gaining attention in recent years  
274 (Wichmann and Peters, 2000), i.e. an increasing number of health effects is attributed rather to  
275 particle number than to particle mass. The fact that NPF-events occur concurrently in or near  
276 the top of the continental planetary boundary layer over wide geographical regions (e.g.,  
277 Wehner et al., 2007) is partly due to concurrent advantageous photochemical conditions  
278 allowing for the formation of condensable vapors, in particular global radiation (Birmili et al.,  
279 2001). Two other factors constraining NPF are the availability of gaseous particle-precursors  
280 and the concurrent pre-existing aerosol.

281

282 The summer map (4-10) of  $N_{10-800}$  exhibits the high values in the Southwest-to-Northeast-  
283 sector of the map. Highest values are concentrated in a belt reaching from Burgundy through  
284 Switzerland, Southern Germany, Czech Republic to Southwestern Poland. Interestingly, this  
285 belt of high  $N_{10-800}$  is collocated to large extent with a belt of high summer ozone concentrations  
286 (cf. Fig. S1). This photochemically controlled pollutant (Monks et al., 2015) exhibits highest  
287 summer concentrations in air masses from Southwestern Poland and Northern Czech Republic,  
288 a region from which high ozone values are reported (Struzewska and Jefimow, 2013; Hůnová,  
289 2003; Hůnová and Bäumelt, 2018). However, the summer map of  $N_{10-800}$  does not show the

290 highest values in air masses from the region with highest ozone pollution. High particle  
291 numbers in air masses coming over the Alps from Northern Italy may be related to the high  
292 emissions of air pollutants in the Po Valley that are known to reach frequently through so called  
293 alpine pumping (Winkler et al., 2006; Lugauer and Winkler, 2005; Reitebuch et al., 2003) over  
294 the mountains. The high NO<sub>x</sub>-concentrations in air masses from Northern Italy in both summer  
295 and winter maps (see Fig. S2) indicate that pollution from south of the Alps can even reach  
296 Northeastern Germany. In the winter map of N<sub>10-800</sub> (11-3 in Fig. 1) the belt of highest summer  
297 values is apparently complemented by more transalpine pollution transport and by transport  
298 from the Southeast. The lower photochemical activity in winter is reflected in the lower winter  
299 ozone concentrations in Fig. S1, albeit transalpine pollution transport is still visible in the winter  
300 map of NO<sub>x</sub> in Fig. S2. Northwestern Italy also shows up as an emission hot spot in the maps  
301 of trajectory-summed emissions in Fig. S4.

302

303 In both summer and winter the maps of PM<sub>10</sub>, and eBC in Fig. 2 exhibit a clear Northwest-  
304 to-Southeast structure with the cleanest sector being in the Northwest covering the coastal area  
305 of the North Sea, the BENELUX countries Belgium, the Netherlands, and Luxemburg, and  
306 Northwestern Germany. The strongest contrast between the cleanest Northwesterly and the  
307 most polluted Southeasterly map sectors is seen in the winter map of eBC. Highest average  
308 concentrations are measured in airmasses from the Southeastern half of the map, most strongly  
309 expressed in PM<sub>10</sub> and eBC with maxima in a region leading from Southwest Poland through  
310 the Czech Republic, Slovakia, Austria, and former Yugoslavia to Northeastern Italy. The back  
311 trajectories in the Southeastern sector of the maps for PM<sub>10</sub> and eBC point towards countries,  
312 in which the emissions of air pollution in the past 20 years developed very differently as  
313 compared to those in Western Europe. According to the European Environment Agency  
314 (<https://www.eea.europa.eu/data-and-maps/dashboards/air-pollutant-emissions-data-viewer-2>)  
315 the latter parts of Western Europe experienced a strong and nearly monotonous decrease in

316 emissions of PM<sub>10</sub> whereas the emissions in Poland, Czech Republic, Slovakia, Austria, former  
317 Yugoslavia, and Italy stayed nearly constant or even increased in recent years after the dramatic  
318 decreases in the course of the political developments of the 1990ies. The seasonal maps of the  
319 combustion derived SO<sub>2</sub> in Fig. S3 look very similar to the those of the particle-mass related  
320 maps of PM<sub>10</sub> and eBC, again the strongest NW/SE-contrast visible in winter.

321

## 322 **5.2. Pollutant emissions and atmospheric processes**

323

324 In Fig. 3 annual average emissions of PM<sub>10</sub>, BC, SO<sub>2</sub>, and NO<sub>x</sub> are mapped for 2009 according  
325 to the EDGAR emission database. Except for the absolute numbers the maps for SO<sub>2</sub>, and NO<sub>x</sub>  
326 look rather similar to those for particulate emissions. They all emphasize highly populated and  
327 industrialized emissions center. Beyond that the SO<sub>2</sub>-map accentuates individual large  
328 combustion sources such as conventional power plants. Whereas the strong emissions in  
329 Northern Italy are seen in the maps of PM<sub>10</sub>, BC, and NO<sub>x</sub> emissions in the countries in the  
330 Southeastern sector of the maps by no means reflect the high concentrations of particulate  
331 components seen in the immission maps of Figs. 1 and 2.

332

333 The seeming discrepancy between the immission maps in Figs. 1 and 2 and the emission  
334 maps of Fig. 3 can be resolved. For that purpose, the EDGAR-emissions of PM<sub>10</sub>, BC, SO<sub>2</sub>,  
335 and NO<sub>x</sub> along all 350593 hourly back trajectories to the four stations during the ten studied  
336 years were summed up. Then the sums were extrapolated back along each trajectory. In Fig.  
337 S4 10-year average maps of these extrapolated emission sums are displayed. As in Fig. 3 except  
338 for the absolute numbers there is a strong similarity between the four mapped component sums.  
339 Because of the integral nature of the mapped results one cannot expect the maps in Fig. S4 to  
340 locate correctly specific emission centers. However, they certainly indicate the map sectors  
341 from which the most substantial emissions could have reached the stations. As in Figs. 1 and

342 2 the Southeastern sectors of the maps of integrated emissions most prominently show up.  
343 Interestingly, the maps in Fig. S4 also indicate the highly polluted region of Northwestern Italy  
344 (Diémoz et al., 2019a; Diémoz et al., 2019b). The emissions from the emission centers in  
345 Northwestern Europe are hardly discernible in Fig. S4. They do show up (most strongly in Fig.  
346 S4c for SO<sub>2</sub>-emission sums) as apparent emissions over the adjacent North Sea. We interpret  
347 the “misplaced” emissions over the North Sea as air mass transport from the North Sea via the  
348 emission region in the BENELUX countries to the receptor sites that was not compensated by  
349 other low pollution air transport from the North Sea to the stations that had not passed over the  
350 Northwestern European emission centers.

351

352 Two major atmospheric processes will reduce the concentrations of emitted or in situ formed  
353 aerosol particles: dilution through mixing with cleaner air masses and wet scavenging through  
354 in-cloud and sub-cloud processes. As a tracer of the first of these two processes Fig. 4a gives  
355 the long-term average geographical distribution of trajectory derived wind speed over the study  
356 area. Highest average wind speeds and ensuing atmospheric mixing is seen over the major  
357 emission centers of Northwestern Germany, the BENELUX countries and adjacent seas  
358 whereas lowest wind speeds are seen over Northern Germany and the Southeastern neighbor  
359 countries. The long-term average geographical distribution of precipitation as taken by  
360 HYSPLIT from the GDAS meteorological fields in Fig. 4b corroborates the results about  
361 atmospheric cleaning processes indicated in Fig. 4a. The small absolute numbers in Fig. 4b are  
362 due to the episodic nature of precipitation: most of the time it does not rain or snow. The blue  
363 crescent reaching from the North Sea through the BENELUX countries, Eastern France,  
364 Switzerland and the alpine region exhibits maximum precipitation values while Southern and  
365 Eastern Germany with the adjoining countries to the East and Southeast show minimum  
366 precipitation values. Thus, in the long term we expect much of the high Western European  
367 emissions to be scavenged to a substantially by wet processes. In addition, air masses arriving

368 from Western and Northwestern directions at the stations usually cross the Western European  
369 emission centers with much lower pollution burdens than air masses coming from the polluted  
370 countries of Southeastern Europe arriving at the corresponding map borders (cf. Fig. PM<sub>10</sub> —  
371 36th maximum daily average value in  $\mu\text{g m}^{-3}$ , 2005 in EEA, 2009).

372

### 373 **5.3. Immission trends for air from specific source regions**

374

375 As mentioned in the introduction, the pollutant emissions reported by the European and national  
376 Environment Agencies represent a synthesis of known pollutant sources combined with  
377 assumed emission factors. These emissions are typically used as input for air quality modelling  
378 and subsequent assessment, as well as for trend analyses. However, it remains unclear to what  
379 extent these reported emissions are realistic, and whether their trends represent the trend in true  
380 emissions. Here, we attempt to assess spatially-resolved trends in real particulate emissions by  
381 an analysis of measured concentrations (immissions) in air masses travelling over source-  
382 specific regions.

383

384 To test our method, we selected two pronounced source regions in Europe, located within  
385 1000 km distance from our observation sites. These regions were defined by emission hotspot  
386 regions that can be seen in the EDGAR emission maps in Fig. 3a-b and comprise: Region A  
387 (Be-NL-NRW; comprising most of Belgium, southern parts of the Netherlands, and much of  
388 the German state North Rhine-Westphalia) and Region B (CZ-PL-SK; comprising the central  
389 parts of the Czech Republic, southern parts of Poland, and adjacent areas of Slovakia.)  
390 According to the European Environment Agency (EEA) these are regions, where reported  
391 particulate emissions have developed differently during the past 10 years. Our goal is to verify  
392 this through an analysis of real atmospheric observations over this period.



393 Temporal trends were computed using the customized Sen–Theil trend estimator (Sen, 1968;  
394 Theil, 1992). The Sen–Theil estimator is the median of many slopes calculated in a continuous  
395 or non-continuous time series, with its robustness against outliers being one of its main assets.  
396 For the detailed description of this trend estimator we refer to Sun et al. (2020), Section 2.3.1.  
397 Here we computed the Sen–Theil estimator for hourly observation data at stations ME, NG,  
398 and WA. Subsets of back trajectories were selected that spent at least 1, 3, 6, or 12 hours over  
399 the source regions A and B. Depending on that criterion, different sub-sets were analyzed. The  
400 difference in median eBC mass concentration between air masses arriving from source region  
401 A and B is obvious, as could already be determined in the corresponding immission maps (Fig.  
402 2c-d). As we learned from Sect. 5.2 these immission maps are strongly influenced by the  
403 different meteorological conditions governing atmospheric dispersion in different wind  
404 direction, so that these values allow no direct conclusion on the strength of emission sources  
405 located upwind.

406

407 We analyzed the temporal trends in eBC over the period 2009-2018 for the subsets belonging  
408 to Regions A and B – assuming that these systematic differences in meteorological conditions  
409 should even out over such long observation periods. Table 2 shows that the Sen–Theil slope  
410 estimator for Region A is between -7.6 % and -5.1 % for the three observation sites and the  
411 requirement of a back trajectory to have spent at least 6 hours over Region A. For region B,  
412 the corresponding Sen–Theil slope estimators are between -4.0 % and -2.7 % for the  
413 observation sites. As we can read from these results, the annual decrease in eBC is more  
414 pronounced for air masses that have travelled over Region A.

415

416 Between 2009 and 2017 for the EU member states of Belgium, the Netherlands, Germany,  
417 the Czech Republic, Poland, and Slovakia the annual rates of decrease in reported emissions  
418 were between -4.9 and -6.1 % for the first three countries, and between +0.5 and -2.8% for the

419 latter three (<https://www.eea.europa.eu/data-and-maps/dashboards/air-pollutant-emissions->  
420 [data-viewer-2](https://www.eea.europa.eu/data-and-maps/dashboards/air-pollutant-emissions-data-viewer-2)). As compiled in Table 2 these reported trends are largely consistent with the  
421 rates of changed derived from our eBC immission trends. Although we need to keep in mind  
422 that the six nation states only partially contribute to our regions A and B, it seems valid to  
423 conclude that BC emissions in region A indeed decreased more rapidly in the past decade  
424 compared to region B. Our approach seems able to differentiate between concentrations trends  
425 in air masses that have passes over rather different source regions. This might represent a step  
426 towards the assessment of changes in real-world emissions allocated in specific source regions  
427 over multi-annual periods.

428

#### 429 **5.4. Comparison of immission and emission trends**

430

431 Besides the map comparison a second approach was used to connect emission data with the  
432 measured aerosol time series. Along each of the hourly back trajectories the emissions  
433 according to the EDGAR database were summed up. Then monthly medians of the emission  
434 sums and the measured parameters were formed. The EDGAR database reports annual average  
435 emissions. PM<sub>10</sub>, black carbon and other combustion related air pollutants show substantial  
436 annual variations with high winter and low summer values at non-urban sites (e.g.,  
437 Heintzenberg and Bussemer, 2000). In emission modeling the temporal variation of annually  
438 reported emissions is considered by disaggregating the annual values with monthly, weekly and  
439 daily factors (Matthias et al., 2018). For the time-resolved comparison of PM<sub>10</sub> and BC-  
440 emissions with PM<sub>10</sub> and eBC-concentrations at the GUAN-sites monthly medians of PM<sub>10</sub> and  
441 eBC-values at the stations were formed and plotted in Fig. 5. We expected both, seasonal  
442 variations and a long-term trend in the emissions. For  $M$  hours per month of measured  
443 components at the four stations the annual average EDGAR-emissions  $E_{PM10}$ ,  $E_{BC}$ ,  $E_{SO2}$ , and  
444  $E_{NOx}$  were summed up along the 121 trajectory steps leading to the stations. Then monthly

445 medians  $\tilde{E}_{i=1,4}$  were formed according to Eq. 1 (exemplified for BC). Medians were chosen to  
446 reduce the effect of outliers due to local emission and scavenging events.

447

$$448 \quad \tilde{E}_{BC} = \text{Median}(\sum_{n=1}^{121} E_{BC})_{m=1,M} \quad \text{Eq. 1}$$

449

450 The monthly median emission sums  $\tilde{E}_{i=1,4}$  were modified with a monthly ( $f_m$ ) and an annual  
451 factor ( $g_y$ ) in order to simulate respective median monthly measured concentrations taken over  
452 all stations. Thus, for each component 12 monthly and 10 annual trend factors determined the  
453 agreement of modified summed emissions and measured concentrations. As objective or utility  
454 function  $\chi^2$  the sum of squared deviations between annually and monthly modified emission  
455 sums and monthly median measured concentrations was formed taken over the 120 months of  
456 the present study (exemplified for BC in Eq. 2).

457

$$458 \quad \chi_{BC}^2 = \sum_{j=1}^{120} (f_{m=1,12} \cdot g_{y=1,10} \cdot \tilde{E}_{BC} - e_{BC})^2 \quad \text{Eq. 2}$$

459

460  $\chi^2$  was minimized with a Generalized Reduced Gradient (GRG) solver (Lasdon et al., 1978)  
461 that optimized the 12 monthly and 10 annual factors for each of the four measured components.  
462 We used Excel's<sup>®</sup> implementation of the GRG-solver procedure for the optimization. After  
463 optimizing month and trend factors the average relative deviation between emission-simulated  
464 and measured monthly median curves is 14%, 21%, 25%, and 18% for PM<sub>10</sub>, eBC, SO<sub>2</sub>, and  
465 NO<sub>x</sub>, and respectively. The optimized monthly median emission sums for all four parameters  
466 are displayed in Fig. 5 together with the measured monthly median concentrations.

467

468 A ten-year trend in emissions of PM<sub>10</sub>, BC, SO<sub>2</sub>, and NO<sub>x</sub>, and average monthly factors for  
469 the respective parameters are the two essential results derived from the optimization approach.

470 The ten-year trends relative to 2009 are collected in Fig. 6. Annual averages of the relative  
471 differences between the monthly median measured parameters and the corresponding emission  
472 derived parameters were formed and applied to the GUAN-trend values displayed in Fig. 6.  
473 The resulting error bars on the trends serve as estimates of the uncertainties of the optimization  
474 approach. The general trend in Fig. 6 is downward to minima between 30 and 70% of the 2009  
475 values in 2016/17 after which all parameters exhibit increases, most strongly PM<sub>10</sub>. SO<sub>2</sub> shows  
476 the strongest decrease whereas PM<sub>10</sub> and NO<sub>x</sub>-emissions diminished the least. In 2010/2011  
477 the trend curves of PM<sub>10</sub> and NO<sub>x</sub> in Fig. 6 show a slight increase that can be linked to a recovery  
478 of economic activity after the world-wide financial and economic crisis during the period 2007-  
479 2009. The increase in PM<sub>10</sub> is also visible in the trend curves relative to  
480 2005 published by the German Environment Agency  
481 ([https://www.umweltbundesamt.de/daten/luft/luftschaedstoff-emissionen-in-](https://www.umweltbundesamt.de/daten/luft/luftschaedstoff-emissionen-in-deutschland/emissionen-prioritaerer-luftschaedstoffe)  
482 [deutschland/emissionen-prioritaerer-luftschaedstoffe](https://www.umweltbundesamt.de/daten/luft/luftschaedstoff-emissionen-in-deutschland/emissionen-prioritaerer-luftschaedstoffe)).

483

484 The results of two comparisons of our trends with data reported by the German and European  
485 Environment Agencies are added to Fig. 6. In general, the trends reported by the German  
486 Environment Agency for all German emissions exhibit weaker reductions than the results of  
487 the present study. Only for PM<sub>10</sub> in 2011 and 2013 the present study yields higher values than  
488 GEA. We note that primary PM<sub>10</sub>-emissions may have substantial contributions from wind  
489 erosion of agricultural soils (Panagos et al., 2015) that are not incorporated in present  
490 anthropogenic inventories. SO<sub>2</sub> exhibits the strongest trend discrepancies with much stronger  
491 reductions in trend of the present study as compared to GEA results. As Germany has been  
492 reducing SO<sub>2</sub> emissions systematically since the nineteen eighties one would not expect any  
493 further strong trends during the time period of the present study. As other studies have  
494 demonstrated before, (e.g., van Pinxteren et al., 2019), the maps in Fig. 1 indicate the possibility  
495 of imported pollution, in particular from the Southeast. Consequently, we searched for similar

496 trends in emission data reported by EEA for neighboring countries until 2017 directly West,  
497 South, and East of Germany, going in the East all the way to Romania. Excel's solver optimized  
498 combinations of the EEA-trends for Germany and neighboring countries in order to fit the  
499 trends derived in the present study. The solver did not choose German trends for any of the  
500 four parameters PM<sub>10</sub>, BC, SO<sub>2</sub>, and NO<sub>x</sub>. For PM<sub>10</sub> a combination of emission trends for the  
501 BENELUX countries and France was optimum, albeit without being able to simulate the  
502 relative maxima in 2011 and 2013 and the minimum around 2016. For BC the emission trend  
503 for the BENELUX countries came closest to the trend of the present study. For SO<sub>2</sub> mostly  
504 emissions in Romania with minor contributions from French and BENELUX trends simulated  
505 the trends observed over Germany best. NO<sub>x</sub>-trends were best simulated by emissions over the  
506 Czech and Slovakian countries. Emissions trends over Switzerland, Austria, Hungary and  
507 Poland were not utilized by the solver. All simulated trends are displayed as curves EEA in  
508 Fig. 6. We do not claim that these simulated trends numerically correspond to imported  
509 pollution over Germany. However, the good fit of SO<sub>2</sub>-trend with emissions over Romania  
510 corroborates our finding of pollution import from Southeastern Europe to Northeastern  
511 Germany while the development of BC appears to follow better emission trends over Western  
512 neighbor countries than over Germany.

513

514 Sun et al., (2020) investigated trends of size resolved number and eBC mass concentrations  
515 at 16 observational sites in Germany from 2009 to 2018 including the three GUAN-sites of the  
516 present study. Based on monthly median time series they report average decreases for ME,  
517 NG, and WA of -5.5%, -6.1, and -3.9%, respectively. The corresponding result for eBC of the  
518 present study is -4.6%, albeit with a high variability (cf. Fig. 6) of 20 percent units expressed  
519 in terms of a standard deviation.

520

521 Over the polluted continent the particle-number based parameter  $N_{10-800}$  is largely secondary  
522 in nature, i.e., its concentrations are controlled by atmospheric constituents and processes.  
523 Thus, there is no primary emission data base with which a similar trend analysis as with  $PM_{10}$ ,  
524  $BC$ ,  $SO_2$ , and  $NO_x$  could be attempted. Instead we chose the 10-year Grand Averages (GA)  
525 averages taken over the whole time period of the present study as references from the deviations  
526 of annual averages are discussed. Sun et al. (2020) report very minor trends (between -3.5%  
527 and 0.1%) for  $N_{20-800}$  at the three GUAN stations of the present study. The 10-year interannual  
528 variation of our  $N_{10-800}$  in Fig. 7a) bears out why only a minor trend if any can be expected. For  
529 the first four years the annual averages are substantially higher than average. Then annual  
530 values decrease down to a minimum in the years 2016/17 before they increase again to a level  
531 slightly above the 10-year average.

532

533 In Figs 7b-d) annual deviations from the respective GAs are displayed that can be connected  
534 to the 10-year course of  $N_{10-800}$ . Ozone concentrations averaged over the data from the three  
535 GUAN stations can be interpreted as an indicator for photochemical activity that also controls  
536 NPF. The annual deviations of  $O_3$  in Fig. 7b) follow rather closely those of  $N_{10-800}$ . In Figs 7c)  
537 and d) annual deviations of ambient temperature and precipitation rates are displayed that have  
538 been averaged over the meteorological data along the back trajectories leading to the four  
539 stations. For the temperature an averaging period of 120 trajectory hours yielded the highest  
540 (negative) correlation with  $N_{10-800}$  of  $r = -0.8$ . After a dip in 2009 annual average trajectory  
541 temperatures to a maximum in 2016 before returning to near average in 2018. For the  
542 precipitation rates along the trajectories the highest (negative) correlation with  $N_{10-800}$  was  
543 found with an averaging period of three days ( $r=-0.6$ ) before arrival at the stations. The results  
544 displayed in Figs 7c) and d) illustrate the complexity of processes and conditions controlling  
545 atmospheric particle number concentrations. On one hand, a scavenging effect of precipitation  
546 can be used as argument for the high values of  $N_{10-800}$  in the years 2010-2013 and the low values

547 in the years 2014 through 2018. On the other hand, lower annual temperatures during years of  
548 relatively high  $N_{10-800}$  and higher than GA-temperatures during years of relatively high  $N_{10-800}$   
549 are harder to interpret. Possibly the nucleation of condensable vapors is furthered by lower air  
550 temperatures upwind of the stations.

551

552 An important result of trend analysis are the average monthly factors disaggregating the  
553 annual emissions. In general the summer minima of the month factors determined in the present  
554 study are broader than the curve given by Matthias et al., (2018) for combustion emissions. The  
555 decrease of the month factor of  $PM_{10}$ , BC, and  $NO_x$  in December and the late winter maxima  
556 of  $PM_{10}$  and  $SO_2$  are not reflected in the Matthias et al., (2018) results. Interestingly, both  $PM_{10}$   
557 and  $SO_2$  show a minor secondary peak in June. As an example of the seasonal variability of  
558 eBC within an urban source region we averaged the relative annual variation of eBC-  
559 concentrations at the station Leipzig Eisenbahnstraße (plotted as curve L-EBS in Fig. 8)  
560 exhibiting a smaller seasonal swing than all other curves. The curve for  $PM_{10}$  comes closest to  
561 that for L-EBS, probably because of agricultural non-combustion emissions in summer.

562

563 In general the downward trends in particulate parameters determined in the present study are  
564 similar to temporal trends of particle number and black carbon mass concentrations at 16  
565 observational sites in Germany from 2009 to 2018 (Sun et al., 2020). The long-term emission-  
566 decrease of  $PM_{10}$  as determined in the present study from 2009 to 2018 is smaller than the  
567 corresponding number published by the EEA as average over all 28 EU member-states but  
568 similar to the figures published by GEA until 2017 (cf. Table 2). For BC,  $SO_2$ , and  $NO_x$  the  
569 present study yields substantially stronger emission-reductions than both GEA and EEA. These  
570 findings are emphasized when considering 2017 as endpoint of the trend calculation (cf. Table  
571 2) at and after which our study shows consistent emission increases of all studied parameters.  
572 Comparing the calculated trends with emission trends in neighboring countries as published by

573 the European Environment Agency supports the explanation that the observed trends are to  
574 some extent due to changes in imported air masses. Most strongly this holds for SO<sub>2</sub>, the trend  
575 of which follows that of Romanian emissions rather well.

576

577 The last issue we take up in this discussion concerns the frequent residual difference between  
578 measured and emission-simulated time series. In Fig. 5, e.g., in most winters there are months  
579 when optimized BC-emissions remain substantially lower than the measured monthly medians  
580 of eBC. Some information can be gleaned from the “Großwetterlagen”, (GWL), representing  
581 29 classifications of large scale weather types after Hess and Brezowsky for Central Europe,  
582 (Gerstengarbe and Werner, 1993), provided by the German Weather service for each day  
583 (<http://www.dwd.de/DE/leistungen/grosswetterlage/grosswetterlage.html>). During the winter  
584 months with the strongest difference between measured and simulated time series the  
585 probabilities of high-pressure systems over Fennoscandia with south-to-southeasterly flow to  
586 the four stations is substantially higher than the respective probabilities averaged over the whole  
587 ten-year period of the study. This GWL-information is consistent with the back trajectories  
588 during the high pollution winter months coming predominantly from the southeasterly sector  
589 of the map. While the classified large-scale weather situation with weak dilution of pollution  
590 during the winter months is conducive of high particulate concentrations at the receptor sites it  
591 does not explain the discrepancy. In principle our simplistic approach of accumulating  
592 emissions along back trajectories may be flawed during certain weather situations. However,  
593 an alternative explanation could be that the emissions inventories over Eastern and Southeastern  
594 Europe in the EDGAR database are somewhat lower than the real emissions.

595

596

597 **6 Summary and conclusions**



598

599 Ten years of hourly aerosol and gas data at three stations of the German Ultrafine Aerosol  
600 Network GUAN and one station of the Saxonian Environment Agency have been combined  
601 with hourly back trajectories to the stations and emission inventories. Measured  $PM_{10}$ , particle  
602 number concentrations between 10 and 800 nm, and equivalent black carbon were extrapolated  
603 along the trajectories. This process yielded what we termed immission maps of these aerosol  
604 parameters over Germany. They reflect aerosol emissions modified with atmospheric processes  
605 along the air mass transport between sources and the four receptor sites at which potential  
606 effects of the particulate air pollution would be realized.

607

608 The ten-year average immission maps do not simply show the distribution of pollution  
609 sources upwind of the receptor sites. The comparison with emission data based on the European  
610 EDGAR emission database shows that strong Western European emission centers do not  
611 dominate the downwind concentrations because their emissions often are reduced by wet  
612 scavenging and dilution processes on the way to the receptor area. Maps of average  
613 precipitation and wind as they occurred along the trajectories illustrate these processes. In the  
614 receptor region mass related aerosol parameters such as  $PM_{10}$ , equivalent black carbon, and to  
615 some extent also the particle number concentration instead is rather controlled by emissions  
616 from Eastern and Southeastern Europe from which pollution transport often occurs under dryer  
617 meteorological conditions in continental high-pressure air masses. This finding corresponds to  
618 the air mass results derived for the sub-micrometer particle number size distribution by Birmili  
619 et al., (2001), by Engler et al., (2007) for the size distribution of non-volatile particles, by Ma  
620 et al., (2014) for optical particle properties all evaluated at the station Melpitz, and by van  
621 Pinxteren et al., (2019) for transboundary transport of  $PM_{10}$  to ten stations in Eastern Germany  
622 from neighboring countries. Newly formed particles on the other hand are found in air masses  
623 from a broad belt reaching from Burgundy to the Western Czech Republic and Southern Poland,

624 a region with high photochemical activity in summer that is affected by emissions in Northern  
625 Italy.

626

627 Annual EDGAR emissions for 2009 of PM<sub>10</sub>, BC, SO<sub>2</sub>, and NO<sub>x</sub>, were accumulated along  
628 each trajectory and compared the calculated emission sums with the corresponding measured  
629 time series on a monthly basis. With a generalized reduced gradient solver the agreement of  
630 each pair of monthly time series e.g., measured eBC and BC-emissions was optimized by letting  
631 the solver determine both monthly emission factors disaggregating the annual EDGAR  
632 emission fields and adjusting the emissions with annual factors modifying the 2009-fields.  
633 Relative to 2009 the annual averages of the analyzed air pollutants were lower in 2018 by values  
634 between 6% for PM<sub>10</sub> and 60% for SO<sub>2</sub>. In general, the ten-year reductions determined of the  
635 present study were stronger than those reported by the German and the European Environmental  
636 Agencies. N<sub>10-800</sub> exhibited substantial interannual variability but no net decrease over the ten  
637 studied years.

638

639 The validity of the present approach of connecting immission and emission of particulate  
640 pollution was tested by calculating temporal changes of eBC for subsets of back trajectories  
641 passing over two separate prominent emission regions, region A to the Northwest and B to the  
642 Southeast of the measuring stations. Consistent with reported emission data the calculated  
643 immission decreases over region A are significantly stronger than over region B.

644

645 Compared to published emission monthly factors by Matthias et al., (2018) the present  
646 approach yielded broader summer minima that were partly displaced from the midsummer  
647 positions given by Matthias et al., (2018). As an aside we note that during the winter months  
648 with extremely high particulate pollution the emissions accumulated along back trajectories

649 often are substantially lower than the measured concentrations which raises the question of the  
650 validity of the emission figures in Eastern and Southeastern European source regions.

651

652 There are clear limits in the methodology of the present study. Air mass trajectories have  
653 inherent uncertainties increasing with their distance travelled (Stohl, 1998). Meteorological  
654 processes affecting the aerosol during air mass transport are only considered rather coarsely  
655 whereas aerosol dynamics are not considered at all. Possible future improvements concern  
656 ensemble trajectories with higher resolution, better meteorological information along the  
657 trajectories e.g., radar-derived precipitation as used in Heintzenberg et al., (2018), more  
658 comprehensive emission inventories with higher spatiotemporal resolution and higher numbers  
659 of analyzed stations.

660

661 Acknowledgements

662

663 This work was accomplished in the framework of the project ACTRIS-2 (Aerosols, Clouds,  
664 and Trace gases Research InfraStructure) under the European Union—Research Infrastructure  
665 Action in the frame of the H2020 program for “Integrating and opening existing national and  
666 regional research infrastructures of European interest” under Grant Agreement N654109,  
667 (H2020—Horizon 2020). Additionally, we acknowledge the WCCAP (World Calibration  
668 Centre for Aerosol Physics) as part of the WMO-GAW program base-funded by the German  
669 Federal Environmental Agency (UBA). Continuous aerosol measurements as well as data  
670 processing at Melpitz, Waldhof and Neuglobsow were supported by the German Federal  
671 Environment Agency Grants F&E 370343200 (German title: “Erfassung der Zahl feiner und  
672 ultrafeiner Partikel in der Außenluft”), and F&E 371143232 (German title: “Trendanalysen  
673 gesundheitsgefährdender Fein-und Ultrafeinstaubfraktionen unter Nutzung der im German  
674 Ultrafine Aerosol Network (GUAN) ermittelten Immissionsdaten durch Fortführung und

675 Interpretation der Messreihen). We gratefully acknowledge receiving the emission data set  
676 from European emission data base for global atmospheric research (EDGAR). We  
677 acknowledge technical support by Annette Pausch of the Saxon State Office for Environment,  
678 Agriculture and Geology at the Collmberg station, Achim Grüner und René Rabe (TROPOS)  
679 at the Melpitz station, by Olaf Bath (GEA) at the Neuglobsow station, and Andreas Schwerin  
680 (GEA) at the Waldhof station. Fabian Senf compiled the “Großwetterlagen” for the present  
681 study. We are most grateful for the ideas provided by Peter Winkler in the interpretation of  
682 data.  
683

684 Literature

685

686 Anderson, J. O., Thundiyil, J. G., and Stolbach, A.: Clearing the air: a review of the effects of  
687 particulate matter air pollution on human health, *J Med Toxicol*, 8, 166-175,  
688 10.1007/s13181-011-0203-1, 2012.

689 Beekmann, M., Prévôt, A. S. H., Drewnick, F., Sciare, J., Pandis, S. N., Denier van der Gon,  
690 H. A. C., Crippa, M., Freutel, F., Poulain, L., Gherzi, V., Rodriguez, E., Beirle, S.,  
691 Zotter, P., von der Weiden-Reinmüller, S. L., Bressi, M., Fountoukis, C., Petetin, H.,  
692 Szidat, S., Schneider, J., Rosso, A., El Haddad, I., Megaritis, A., Zhang, Q. J., Michoud,  
693 V., Slowik, J. G., Moukhtar, S., Kolmonen, P., Stohl, A., Eckhardt, S., Borbon, A., Gros,  
694 V., Marchand, N., Jaffrezo, J. L., Schwarzenboeck, A., Colomb, A., Wiedensohler, A.,  
695 Borrmann, S., Lawrence, M., Baklanov, A., and Baltensperger, U.: In situ, satellite  
696 measurement and model evidence on the dominant regional contribution to fine  
697 particulate matter levels in the Paris megacity, *Atmos. Chem. Phys.*, 15, 9577-9591,  
698 10.5194/acp-15-9577-2015, 2015.

699 Birmili, W., Wiedensohler, A., Heintzenberg, J., and Lehmann, K.: Atmospheric particle  
700 number size distribution in Central Europe: Statistical relations to air masses and  
701 meteorology, *J. Geophys. Res.*, 106, 32005-32018, 2001.

702 Birmili, W., Weinhold, K., Merkel, M., Rasch, F., Sonntag, A., Wiedensohler, A., Bastian, S.,  
703 Schladitz, A., Löschau, G., Cyrys, J., Pitz, M., Gu, J., Kusch, T., Flentje, H., Quass, U.,  
704 Kaminski, H., Kuhlbusch, T. A. J., Meinhardt, F., Schwerin, A., Bath, O., Ries, L.,  
705 Wirtz, K., and Fiebig, M.: Long-term observations of tropospheric particle number size  
706 distributions and equivalent black carbon mass concentrations in the German Ultrafine  
707 Aerosol Network (GUAN), *Earth Syst. Sci. Data*, 8, 355-382, doi:10.5194/essd-8-355-  
708 2016, 2016.

709 Bond, T. C., Doherty, S. J., Fahey, D. W., Forster, P. M., Berntsen, T., DeAngelo, B. J., Flanner,  
710 M. G., Ghan, S., Kärcher, B., Koch, D., Kinne, S., Kondo, Y., Quinn, P. K., Sarofim,  
711 M. C., Schultz, M. G., Schulz, M., Venkataraman, C., Zhang, H., Zhang, S., Bellouin,  
712 N., Guttikunda, S. K., Hopke, P. K., Jacobson, M. Z., Kaiser, J. W., Klimont, Z.,  
713 Lohmann, U., Schwarz, J. P., Shindell, D., Storelvmo, T., Warren, S. G., and Zender,  
714 C. S.: Bounding the role of black carbon in the climate system: A scientific assessment,  
715 *J. Geophys. Res.*, doi: 10.1002/jgrd.50171, [10.1002/jgrd.50171](https://doi.org/10.1002/jgrd.50171), 2013.

716 Cass, G. R., and McRae, G. J.: Source-receptor reconciliation of routine air monitoring data for  
717 trace metals: An emission inventory assisted approach, *Environ. Sci. Technol.*, 17, 129-  
718 139, 1983.

719 Charron, A., Birmili, W., and Harrison, R. M.: Fingerprinting particle origins according to their  
720 size distribution at a UK rural site, *J. Geophys. Res.*, 113, D07202,  
721 doi:07210.01029/02007JD008562, 2008.

722 Crippa, M., Guizzardi, D., Muntean, M., Schaaf, E., Dentener, F., van Aardenne, J. A., Monni,  
723 S., Doering, U., Olivier, J. G. J., Pagliari, V., and Janssens-Maenhout, G.: Gridded  
724 emissions of air pollutants for the period 1970–2012 within EDGAR v4.3.2, *Earth Syst.*  
725 *Sci. Data*, 10, 1987-2013, [10.5194/essd-10-1987-2018](https://doi.org/10.5194/essd-10-1987-2018), 2018.

726 Diémoz, H., Barnaba, F., Magri, T., Pession, G., Dionisi, D., Pittavino, S., Tombolato, I. K. F.,  
727 Campanelli, M., Della Ceca, L. S., Hervo, M., Di Liberto, L., Ferrero, L., and Gobbi, G.  
728 P.: Transport of Po Valley aerosol pollution to the northwestern Alps – Part 1:  
729 Phenomenology, *Atmos. Chem. Phys.*, 19, 3065-3095, [10.5194/acp-19-3065-2019](https://doi.org/10.5194/acp-19-3065-2019),  
730 2019a.

731 Diémoz, H., Gobbi, G. P., Magri, T., Pession, G., Pittavino, S., Tombolato, I. K. F., Campanelli,  
732 M., and Barnaba, F.: Transport of Po Valley aerosol pollution to the northwestern Alps  
733 – Part 2: Long-term impact on air quality, *Atmos. Chem. Phys.*, 19, 10129-10160,  
734 [10.5194/acp-19-10129-2019](https://doi.org/10.5194/acp-19-10129-2019), 2019b.

735 Draxler, R., and Hess, G.: An overview of the HYSPLIT\_4 modeling system for trajectories,  
736 dispersion, and deposition, *Austr. Meteor. Mag.*, 47, 295-308, 1998.

737 EEA: Spatial assessment of PM<sub>10</sub> and ozone concentrations in Europe (2005), European  
738 Environmental Agency, Copenhagen, Denmark, 52 pp, 2009.

739 Eliassen, A.: The OECD Study of Long Range Transport of Air Pollutants: Long Range  
740 Transport Modelling, *Atmos. Environ.*, 12, 479-487, 1978.

741 Engler, C., Rose, D., Wehner, B., Wiedensohler, A., Brüggemann, E., Gnauk, T., Spindler, G.,  
742 Tuch, T., and Birmili, W.: Size distributions of non-volatile particle residuals (Dp<800  
743 nm) at a rural site in Germany and relation to air mass origin, *Atmos. Chem. Phys.*, 7,  
744 5785-5802, 10.5194/acp-7-5785-2007, 2007.

745 Friedlander, S. K.: Chemical element balances and identification of air pollution sources, *Env.*  
746 *Sci. & Technol.*, 7, 235-240, 10.1021/es60075a005, 1973.

747 Gerstengarbe, F.-W., and Werner, P. C.: Katalog der Grosswetterlagen Europas nach Paul Hess  
748 und Helmut Brezowski 1881-1992, 4., vollständ. neu bearb. Aufl., Deutscher  
749 Wetterdienst, Offenbach, Germany, 1993.

750 Heintzenberg, J., and Bussemer, M.: Development and application of a spectral light absorption  
751 photometer for aerosol and hydrosol samples, *J. Aerosol Sci.*, 31, 801-812, 2000.

752 Heintzenberg, J., Birmili, W., Seifert, P., Panov, A., Chi, X., and Andreae, M. O.: Mapping the  
753 aerosol over Eurasia from the Zotino Tall Tower (ZOTTO), *Tellus B*, 65,  
754 doi:<http://dx.doi.org/10.3402/tellusb.v3465i3400.20062>, 2013.

755 Heintzenberg, J., Leck, C., and Tunved, P.: Potential source regions and processes of aerosol  
756 in the summer Arctic, *Atmos. Chem. Phys.*, 15, 6487-6502, 10.5194/acp-15-6487-2015,  
757 2015.

758 Heintzenberg, J., Senf, F., Birmili, W., and Wiedensohler, A.: Aerosol connections between  
759 distant continental stations, *Atmos. Environ.*, 190, 349-358, 2018.

760 Hůnová, I.: Ambient air quality for the territory of the Czech Republic in 1996–1999 expressed  
761 by three essential factors, *Sci. Total Environ.*, 303, 245-251,  
762 [https://doi.org/10.1016/S0048-9697\(02\)00493-X](https://doi.org/10.1016/S0048-9697(02)00493-X), 2003.

763 Hůnová, I., and Bäumelt, V.: Observation-based trends in ambient ozone in the Czech Republic  
764 over the past two decades, *Atmos. Environ.*, 172, 157-167,  
765 <https://doi.org/10.1016/j.atmosenv.2017.10.039>, 2018.

766 Kanamitsu, M.: Description of the NMC Global Data Assimilation and Forecast System, *Wea.*  
767 *Forecasting*, 4, 335-342, 10.1175/1520-0434(1989)004<0335:DOTNGD>2.0.CO;2,  
768 1989.

769 Klimont, Z., Kupiainen, K., Heyes, C., Purohit, P., Cofala, J., Rafaj, P., Borcken-Kleefeld, J.,  
770 and Schöpp, W.: Global anthropogenic emissions of particulate matter including black  
771 carbon, *Atmos. Chem. Phys.*, 17, 8681-8723, 10.5194/acp-17-8681-2017, 2017.

772 Krige, D. G.: A statistical approach to some basic mine valuation problems on the  
773 Witwatersrand, *J. Chem. Metall. Min. Soc. S. Afr.*, December, 119-159, 1951.

774 Kuenen, J. J. P., Visschedijk, A. J. H., Jozwicka, M., and Denier van der Gon, H. A. C.: TNO-  
775 MACC\_II emission inventory; a multi-year (2003 - 2009) consistent high-resolution  
776 European emission inventory for air quality modelling, *Atmos. Chem. Phys.*, 14, 10963-  
777 10976, 10.5194/acp-14-10963-2014, 2014.

778 Kulmala, M., Vehkamäkia, H., Petäjä, T., Dal Maso, M., Lauri, A., Kerminen, V.-M., Birmili,  
779 W., and McMurry, P. H.: Formation and growth rates of ultrafine atmospheric particles:  
780 a review of observations, *J. Aerosol Sci.*, 35, 143-176, 2004.

781 Lasdon, L. S., Waren, A. D., Jain, A., and Ratner, M.: Design and Testing of a Generalized  
782 Reduced Gradient Code for Nonlinear Programming, *ACM Trans. Math. Softw.*, 4, 34–  
783 50, 10.1145/355769.355773, 1978.



784 Lavanchy, V. M. H., Gäggeler, H. W., Schotterer, U., Schwikowski, M., and Baltensperger, U.:  
785 Historical record of carbonaceous particle concentrations from a European high-alpine  
786 glacier (Colle Gnifetti, Switzerland), *J. Geophys. Res.*, 104, 21227-21236, 1999.

787 Leibensperger, E. M., Mickley, L. J., Jacob, D. J., Chen, W. T., Seinfeld, J. H., Nenes, A.,  
788 Adams, P. J., Streets, D. G., Kumar, N., and Rind, D.: Climatic effects of 1950 - 2050  
789 changes in US anthropogenic aerosols - Part 1: Aerosol trends and radiative forcing,  
790 *Atmos. Chem. Phys.*, 12, 3333-3348, 10.5194/acp-12-3333-2012, 2012.

791 Lelieveld, J., Evans, J. S., Fnais, M., Giannadaki, D., and Pozzer, A.: The contribution of  
792 outdoor air pollution sources to premature mortality on a global scale, *Nature*, 525, 367-  
793 371, 10.1038/nature15371, 2015.

794 Li, Z., Niu, F., Fan, J., Liu, Y., Rosenfeld, D., and Ding, Y.: Long-term impacts of aerosols on  
795 the vertical development of clouds and precipitation, *Nature Geosci.*, 4, 888-894, 2011.

796 Liu, S., Hua, S., Wang, K., Qiu, P., Liu, H., Wu, B., Shao, P., Liu, X., Wu, Y., Xue, Y., Hao,  
797 Y., and Tian, H.: Spatial-temporal variation characteristics of air pollution in Henan of  
798 China: Localized emission inventory, WRF/Chem simulations and potential source  
799 contribution analysis, *Sci. Total Environ.*, 624, 396-406,  
800 <https://doi.org/10.1016/j.scitotenv.2017.12.102>, 2018.

801 Lugauer, M., and Winkler, P.: Thermal circulation in South Bavaria – climatology and synoptic  
802 aspects, *Meteor. Z.*, 14, 15-30, 2005.

803 Ma, N., Birmili, W., Müller, T., Tuch, T., Cheng, Y. F., Xu, W. Y., Zhao, C. S., and  
804 Wiedensohler, A.: Tropospheric aerosol scattering and absorption over central Europe:  
805 a closure study for the dry particle state, *Atmos. Chem. Phys.*, 14, 6241-6259,  
806 10.5194/acp-14-6241-2014, 2014.

807 Marmer, E., and Langmann, B.: Aerosol modeling over Europe: 1. Interannual variability of  
808 aerosol distribution, *J. Geophys. Res.*, 112, D23S15, doi:10.1029/2006JD008113, 2007.

809 Matthias, V., Arndt, J. A., Aulinger, A., Bieser, J., Denier van der Gon, H., Kranenburg, R.,  
810 Kuenen, J., Neumann, D., Pouliot, G., and Quante, M.: Modeling emissions for three-  
811 dimensional atmospheric chemistry transport models, *Journal of the Air & Waste*  
812 *Management Association*, 68, 763-800, 10.1080/10962247.2018.1424057, 2018.

813 Miller, M. S., Friedlander, S. K., and Hidy, G. M.: A chemical element balance for the Pasadena  
814 aerosol, *J. Colloid Interface Sci.*, 39, 165-176, [https://doi.org/10.1016/0021-](https://doi.org/10.1016/0021-9797(72)90152-X)  
815 [9797\(72\)90152-X](https://doi.org/10.1016/0021-9797(72)90152-X), 1972.

816 Minkos, A., Dauert, U., Feigenspan, S., and Kessinger, S.: . German Environment Agency, Jan  
817 2019, D-06813 , 28 pp. , Accessed on September 6, 2019 [Online] Available:  
818 [https://www.umweltbundesamt.de/sites/default/files/medien/1410/publikationen/1903](https://www.umweltbundesamt.de/sites/default/files/medien/1410/publikationen/190329_uba_hg_luftqualitaet_engl_bf.pdf)  
819 [29\\_uba\\_hg\\_luftqualitaet\\_engl\\_bf.pdf](https://www.umweltbundesamt.de/sites/default/files/medien/1410/publikationen/190329_uba_hg_luftqualitaet_engl_bf.pdf): Air Quality 2018 - Preliminary Evaluation,  
820 German Environment Agency, Dessau-Rosslau, Germany, 28, 2019.

821 Monks, P. S., Archibald, A. T., Colette, A., Cooper, O., Coyle, M., Derwent, R., Fowler, D.,  
822 Granier, C., Law, K. S., Mills, G. E., Stevenson, D. S., Tarasova, O., Thouret, V., von  
823 Schneidemesser, E., Sommariva, R., Wild, O., and Williams, M. L.: Tropospheric ozone  
824 and its precursors from the urban to the global scale from air quality to short-lived  
825 climate forcer, *Atmos. Chem. Phys.*, 15, 8889-8973, 10.5194/acp-15-8889-2015, 2015.

826 Müller, T., Henzing, J. S., de Leeuw, G., Wiedensohler, A., Alastuey, A., Angelov, H., Bizjak,  
827 M., Collaud Coen, M., Engström, J. E., Gruening, C., Hillamo, R., Hoffer, A., Imre, K.,  
828 Ivanow, P., Jennings, G., Sun, J. Y., Kalivitis, N., Karlsson, H., Komppula, M., Laj, P.,  
829 Li, S. M., Lunder, C., Marinoni, A., Martins dos Santos, S., Moerman, M., Nowak, A.,  
830 Ogren, J. A., Petzold, A., Pichon, J. M., Rodriguez, S., Sharma, S., Sheridan, P. J.,  
831 Teinilä, K., Tuch, T., Viana, M., Virkkula, A., Weingartner, E., Wilhelm, R., and Wang,  
832 Y. Q.: Characterization and intercomparison of aerosol absorption photometers: result  
833 of two intercomparison workshops, *Atmos. Meas. Tech.*, 4, 245-268, [10.5194/amt-4-](https://doi.org/10.5194/amt-4-245-2011)  
834 [245-2011](https://doi.org/10.5194/amt-4-245-2011), 2011.

835 Nordmann, S., Birmili, W., Weinhold, K., Müller, K., Spindler, G., and Wiedensohler, A.:  
836 Measurements of the mass absorption cross section of atmospheric soot particles using  
837 Raman spectroscopy, *J. Geophys. Res.*, 118, 12,075-012,085, 10.1002/2013JD020021,  
838 2013.

839 Panagos, P., Borrelli, P., Poesen, J., Ballabio, C., Lugato, E., Meusburger, K., Montanarella,  
840 L., and Alewell, C.: The new assessment of soil loss by water erosion in Europe,  
841 *Environmental Science & Policy*, 54, 438-447, 10.1016/j.envsci.2015.08.012, 2015.

842 Patashnick, H., and Rupprecht, E. G.: Continuous PM-10 Measurements Using the Tapered  
843 Element Oscillating Microbalance, *Journal of the Air & Waste Management*  
844 *Association*, 41, 1079-1083, 10.1080/10473289.1991.10466903, 1991.

845 Penner, J. E., Dong, X., and Chen, Y.: Observational evidence of a change in radiative forcing  
846 due to the indirect aerosol effect, *Nature*, 427, 231-234, 2004.

847 Petzold, A., Ogren, J. A., Fiebig, M., Laj, P., Li, S. M., Baltensperger, U., Holzer-Popp, T.,  
848 Kinne, S., Pappalardo, G., Sugimoto, N., Wehrli, C., Wiedensohler, A., and Zhang, X.  
849 Y.: Recommendations for reporting "black carbon" measurements, *Atmos. Chem.*  
850 *Phys.*, 13, 8365-8379, 10.5194/acp-13-8365-2013, 2013.

851 Pruppacher, H. R., and Klett, J. D.: *Microphysics of Clouds and Precipitation*, Reidel Publishing  
852 Co., Dordrecht, 714pp, 1978.

853 Rehme, R.: Application of Gas Phase Titration in the Calibration of Nitric Oxide, Nitrogen  
854 Dioxide, and Ozone Analyzers, in: *Calibration in Air Monitoring*, edited by: Chapman,  
855 R., and Sheesley, D., ASTM International, West Conshohocken, PA, 198-209, 1976.

856 Reitebuch, O., Dabas, A., Delville, P., Drobinsk, P., and Gantner, L.: Characterization of Alpine  
857 pumping by airborne Doppler lidar and numerical simulations., *Int. Conf. Alp. Meteor.*,  
858 *Brig 2003. – Publications of MeteoSwiss*, 66, 134-137, 2003.

859 Riemer, N., Vogel, H., and Vogel, B.: Soot aging time scales in polluted regions during day  
860 and night, *Atmos. Chem. Phys.*, 4, 1885-1893, 2004.

861 Rohde, R. A., and Muller, R. A.: Air Pollution in China: Mapping of Concentrations and  
862 Sources, *PLoS One*, 10, e0135749-e0135749, 10.1371/journal.pone.0135749, 2015.

863 Samset, B. H., Sand, M., Smith, C. J., Bauer, S. E., Forster, P. M., Fuglestedt, J. S., Osprey,  
864 S., and Schleussner, C. F.: Climate Impacts From a Removal of Anthropogenic Aerosol  
865 Emissions, *Geophysical Research Letters*, 45, 1020-1029, 10.1002/2017gl076079,  
866 2018.

867 Schell, B., Ackermann, I., Hass, H., Binkowski, F., and Ebel, A.: Modeling the formation of  
868 secondary organic aerosol within a comprehensive air quality model system, *J.*  
869 *Geophys. Res.*, 106, 28275–28293, 2001.

870 Schwartz, S. E.: The whitehouse effect - shortwave radiative forcing of climate by  
871 anthropogenic aerosols: an overview, *J. Aerosol Sci.*, 27, 359-382, 1996.

872 Sen, P. K.: Estimates of the Regression Coefficient Based on Kendall's Tau, *J. Am. Stat.*  
873 *Assoc.*, 63, 1379–1389, 1968.

874 Spindler, G., Müller, K., and Herrmann, H.: Main particulate matter components in Saxony  
875 (Germany) - trends and sampling aspects, *Environ. Sci. Pollut. Res.*, 6, 89-94, 1999.

876 Spindler, G., Grüner, A., Müller, K., Schlimper, S., and Herrmann, H.: Long-term size-  
877 segregated particle (PM10, PM2.5, PM1) characterization study at Melpitz -- influence  
878 of air mass inflow, weather conditions and season, *J. Atmos. Chem.*, 70, 165-195,  
879 10.1007/s10874-013-9263-8, 2013.

880 Stein, A. F., Draxler, R. R., Rolph, G. D., Stunder, B. J. B., Cohen, M. D., and Ngan, F.:  
881 NOAA's HYSPLIT Atmospheric Transport and Dispersion Modeling System, *Bull.*  
882 *Amer. Meteor. Soc.*, 96, 2059-2077, 10.1175/BAMS-D-14-00110.1, 2015.

883 Stohl, A.: Trajectory statistics - a new method to establish source-receptor relationships of air  
884 pollutants and its application to the transport of particulate sulfate in Europe, *Atmos.*  
885 *Environ.*, 30, 579-587, 1996.

886 Stohl, A.: Computations, accuracy and applications of trajectories - A review and bibliography,  
887 Atmos. Environ., 32, 947-966, 1998.

888 Struzewska, J., and Jefimow, M.: A 15-year analysis of surface ozone pollution in the context  
889 of hot spells episodes over Poland, Acta Geophysica, 64, 1875-1902, 10.1515/acgeo-  
890 2016-0067, 2013.

891 Sun, J., Birmili, W., Hermann, M., Tuch, T., Weinhold, K., Spindler, G., Schladitz, A., Bastian,  
892 S., Löschau, G., Cyrys, J., Gu, J., Flentje, H., Briel, B., Asbach, C., Kaminski, H., Ries,  
893 L., Sohmer, R., Gerwig, H., Wirtz, K., Meinhardt, F., Schwerin, A., Bath, O., Ma, N.,  
894 and Wiedensohler, A.: Variability of Black Carbon Mass Concentrations, Sub-  
895 micrometer Particle Number Concentrations and Size Distributions: Results of the  
896 German Ultrafine Aerosol Network Ranging from City Street to High Alpine Locations,  
897 Atmos. Environ., 202, 256-268, <https://doi.org/10.1016/j.atmosenv.2018.12.029>, 2019.

898 Sun, J., Birmili, W., Hermann, M., Tuch, T., Weinhold, K., Merkel, M., Rasch, F., Müller, T.,  
899 Schladitz, A., Bastian, S., Löschau, G., Cyrys, J., Gu, J., Flentje, H., Briel, B., Asbach,  
900 C., Kaminski, H., Ries, L., Sohmer, R., Gerwig, H., Wirtz, K., Meinhardt, F., Schwerin,  
901 A., Bath, O., Ma, N., and Wiedensohler, A.: Decreasing Trends of Particle Number and  
902 Black Carbon Mass Concentrations at 16 Observational Sites in Germany from 2009 to  
903 2018, Atmos. Chem. Phys., 2019, 1-19, 10.5194/acp-2019-754, 2020.

904 Swietlicki, E., Svantesson, B., and Hansson, H.-C.: European source area apportionment, J.  
905 Aerosol Sci., 19, 1175-1178, 1988.

906 Theil, H.: A Rank-Invariant Method of Linear and Polynomial Regression Analysis, in: Henri  
907 Theil's Contributions to Economics and Econometrics: Econometric Theory and  
908 Methodology, edited by: Raj, B., and Koerts, J., Springer Netherlands, Dordrecht, 345–  
909 381, 1992.

910 Twomey, S.: Pollution and the planetary albedo, Atmos. Environ., 8, 1251-1256, 1974.

911 van Pinxteren, D., Mothes, F., Spindler, G., Fomba, K. W., and Herrmann, H.: Trans-boundary  
912 PM10: Quantifying impact and sources during winter 2016/17 in eastern Germany,  
913 Atmos. Environ., 200, 119-130, <https://doi.org/10.1016/j.atmosenv.2018.11.061>, 2019.

914 Wehner, B., Siebert, H., Stratmann, F., Tuch, T., Wiedensohler, A., Petäjä, T., Dal Maso, M.,  
915 and Kulmala, M.: Horizontal homogeneity and vertical extent of new particle formation  
916 events, *Tellus*, 59 B, 362-371, 2007.

917 Wichmann, H. E., and Peters, A.: Epidemiological evidence of the effects of ultrafine particle  
918 exposure, *Philosophical Transactions of the Royal Society of London*, 358, 1751-2769,  
919 2000.

920 Wiedensohler, A., Birmili, W., Nowak, A., Sonntag, A., Weinhold, K., Merkel, M., Wehner,  
921 B., Tuch, T., Pfeifer, S., Fiebig, M., Fjåraa, A. M., Asmi, E., Sellegri, K., Depuy, R.,  
922 Venzac, H., Villani, P., Laj, P., Aalto, P., Ogren, J. A., Swietlicki, E., Williams, P.,  
923 Roldin, P., Quincey, P., Hüglin, C., Fierz-Schmidhauser, R., Gysel, M., Weingartner,  
924 E., Riccobono, F., Santos, S., Gruning, C., Faloon, K., Beddows, D., Harrison, R.,  
925 Monahan, C., Jennings, S. G., O'Dowd, C. D., Marinoni, A., Horn, H. G., Keck, L.,  
926 Jiang, J., Scheckman, J., McMurry, P. H., Deng, Z., Zhao, C. S., Moerman, M., Henzing,  
927 B., de Leeuw, G., Lösschau, G., and Bastian, S.: Mobility particle size spectrometers:  
928 harmonization of technical standards and data structure to facilitate high quality long-  
929 term observations of atmospheric particle number size distributions, *Atmos. Meas.*  
930 *Tech.*, 5, 657-685, [10.5194/amt-5-657-2012](https://doi.org/10.5194/amt-5-657-2012), 2012.

931 Wiedensohler, A., Wiesner, A., Weinhold, K., Birmili, W., Hermann, M., Merkel, M., Müller,  
932 T., Pfeifer, S., Schmidt, A., Tuch, T., Velarde, F., Quincey, P., Seeger, S., and Nowak,  
933 A.: Mobility particle size spectrometers: Calibration procedures and measurement  
934 uncertainties, *Aerosol Sci. Technol.*, 52, 146-164, [10.1080/02786826.2017.1387229](https://doi.org/10.1080/02786826.2017.1387229),  
935 2018.

936 Winkler, P., Lugauer, M., and Reitebuch, O.: Alpine Pumping, *PROMET*, 32, 34-42, 2006.

937 Wolke, R., Hellmuth, O., Knoth, O., Schröder, W., Heinrich, B., and Renner, E.: The chemistry-  
938 transport modeling system LM-MUSCAT: Description and CityDelta applications, in:  
939 Air Pollution Modeling and its Application XVI, Kluwer Academic/Plenum, 427–439,  
940 2004.

941 Zanatta, M., Gysel, M., Bukowiecki, N., Müller, T., Weingartner, E., Areskoug, H., Fiebig, M.,  
942 Yttri, K. E., Mihalopoulos, N., Kouvarakis, G., Beddows, D., Harrison, R. M., Cavalli,  
943 F., Putaud, J. P., Spindler, G., Wiedensohler, A., Alastuey, A., Pandolfi, M., Sellegri,  
944 K., Swietlicki, E., Jaffrezo, J. L., Baltensperger, U., and Laj, P.: A European aerosol  
945 phenomenology-5: Climatology of black carbon optical properties at 9 regional  
946 background sites across Europe, *Atmos. Environ.*, 145, 346-364,  
947 [10.1016/j.atmosenv.2016.09.035](https://doi.org/10.1016/j.atmosenv.2016.09.035), 2016.

948 Zhu, K., Zhang, J., and Li, P. J.: Evaluation and Comparison of Continuous Fine Particulate  
949 Matter Monitors for Measurement of Ambient Aerosols, *Journal of the Air & Waste  
950 Management Association*, 57, 1499-1506, [10.3155/1047-3289.57.12.1499](https://doi.org/10.3155/1047-3289.57.12.1499), 2007.

951

952 Table 1: Characteristics of the four stations of the present study, see text for instrumental details. The number of validated data hours are  
 953 given for each component

Station	Acronym	Latitude	Longitude	MPSS <sup>1</sup>	eBC <sup>2</sup>	PM10 continuous <sup>3,4</sup>	PM10 discontinuous <sup>5</sup>	NO <sub>x</sub> <sup>6</sup>	SO <sub>2</sub> <sup>7</sup>	O <sub>3</sub> <sup>8</sup>
Collmberg	CO	51.3	13			85054		88838		88792
Melpitz	ME	51.5	12.9	81561	88196		88822	86260	85541	84421
Neuglobsow	NG	53.1	13	57962	77540	71202		83718	87778	87943
Waldhof	WA	52.8	10.8	84276	80725	88321		85503	82386	87373

<sup>1</sup>MPSS - scanning mobility particle size spectrometer TROPOS (10 – 800 nm); <sup>2</sup>MAAP - Multi-angle absorption photometer 5012 Thermo Fischer Scientific; <sup>3</sup>TEOM-FDM - Tapered element oscillating microbalance fitted with a filter dynamics measuring system 1405 Thermo Fischer Scientific; <sup>4</sup>SCHARP - Synchronized Hybrid Ambient Real-time Particulate Monitor 5030 Thermo Fischer Scientific; <sup>5</sup>HVS – High Volume Sampler DIGITEL DH-80; <sup>6</sup>TLA-NOx –Trace Level NOx Analyzer 42i-TL Thermo Fischer Scientific; <sup>7</sup>TLA-SO2 - Trace Level SO<sub>2</sub> Analyzer 43i-TLE Thermo Fischer Scientific; <sup>8</sup>

954

955



956 Table 2 Median concentrations of eBC concentrations ( $\mu\text{g m}^{-3}$ ) and temporal trends (2009-2018) of eBC in terms of Sen-Theil slope (% per year) as  
 957 determined for air masses passing over Regions A and B as analyzed at the stations Melpitz (ME), Neuglobsow (NG), and Waldhof (WA). For  
 958 comparison the national annual decreases in BC emissions 2009-2017 in % according to the European Environmental Agency are added.

	DELTA T* in h	No. of back trajectories			Median eBC in $\mu\text{m}^3$			Sen-Theil slope in % per year			3 Stations**	Decrease in national BC emissions in % per year		
		ME	NG	WA	ME	NG	WA	ME	NG	WA		Belgium	Netherlands	Germany
Region A B-NL-NRW	1	21941	17514	27218	0.38	0.40	0.41	6.40	6.80	4.80	-5.85	-6.1%	-6.1%	-4.9%
	3	18605	14268	22132	0.38	0.40	0.41	6.40	6.90	4.80	-5.89			
	6	14802	10086	15936	0.39	0.40	0.42	6.40	7.60	5.10	-6.19			
	12	6817	3746	6131	0.40	0.50	0.50	7.10	7.90	5.30	-6.62			
Region B CZ-PL-SK	1	11096	5264	4191	1.10	1.19	1.13	3.60	3.40	1.70	-3.16	-2.8%	0.5%	-2.3%
	3	9601	4339	3541	1.08	1.18	1.12	3.40	3.40	2.10	-3.14			
	6	7000	3062	2570	1.05	1.09	1.11	4.00	2.90	2.70	-3.47			
	12	3628	1410	1277	1.00	1.00	1.00	3.70	3.00	2.70	-3.34			
ALL		85846	75190	78356	0.45	0.36	0.36	5.90	5.60	4.00	-5.18			
Sun (2020)								4.40	7.80	3.20				

959 \* Minimum time spent over the specified source region, \*\*Weighted mean, according to the available number of back trajectories

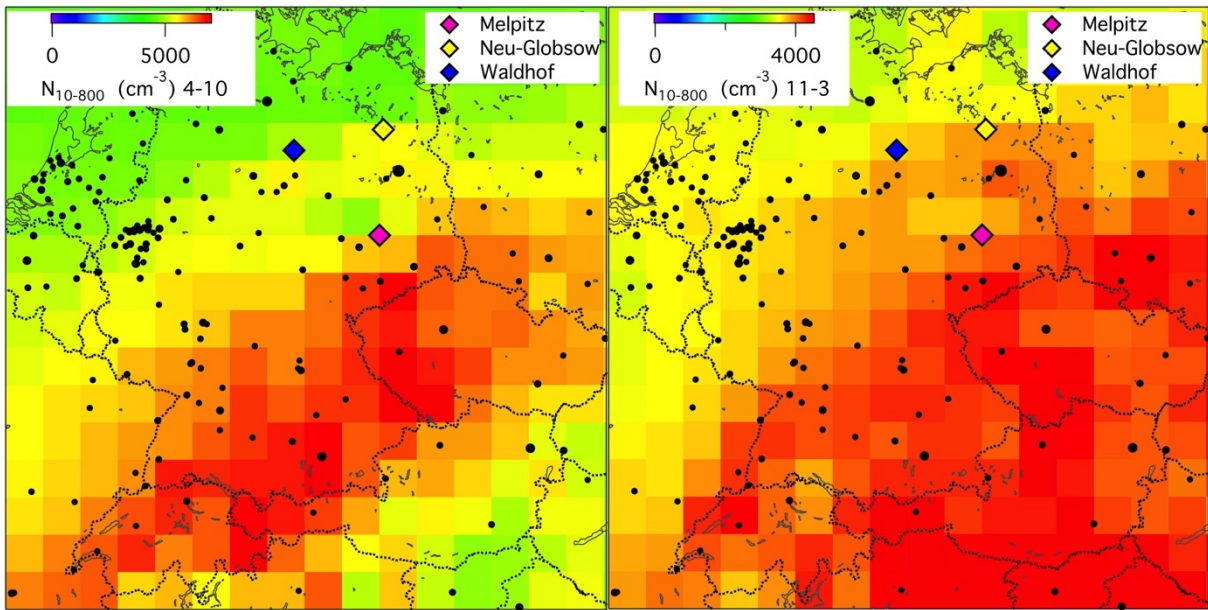
960 Table 3 Percental decreases in the anthropogenic emissions of PM<sub>10</sub>, BC, SO<sub>2</sub>, and  
 961 NO<sub>x</sub> relative to 2009 as reported by the European Environment Agency (EEA,  
 962 [https://www.eea.europa.eu/data-and-maps/dashboards/air-pollutant-emissions-data-  
 963 viewer-2](https://www.eea.europa.eu/data-and-maps/dashboards/air-pollutant-emissions-data-viewer-2)), the German Environment Agency (GEA), and calculated in the present  
 964 study. The EEA and GEA only report data until 2017, (\*=BC until 2016).

965

Component	EEA	GEA	GUAN	GUAN
	2009- 2017	2009- 2017	emissions 2009- 2017	emissions 2009- 2018
PM <sub>10</sub>	12%	4.2%	16%	6%
BC*	29%	35%*	63%	44%
SO <sub>2</sub>	33%	20%	68%	59%
NO <sub>x</sub>	20%	11%	43%	30%

966

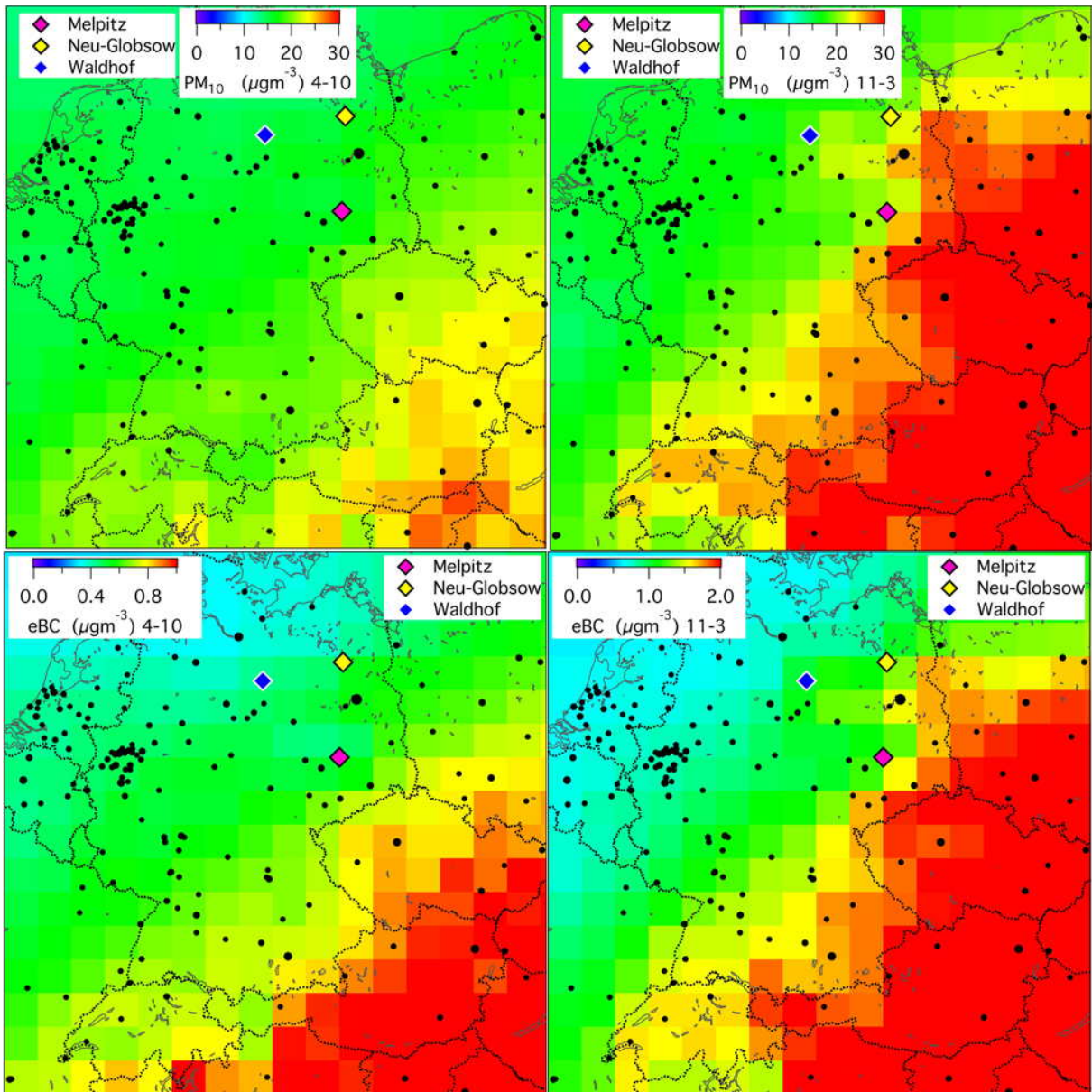
967



968

969 Fig. 1 Maps of particle number concentration  $N_{10-800}$  ( $\text{cm}^{-3}$ ) extrapolated under 1000 m height  
 970 along five day back trajectories from hourly data at the four stations from 2009 to 2018;  
 971 left: months April through October; right: months November through March. The  
 972 GUAN-stations are marked with colored diamonds. The Collmberg station lies 30 km  
 973 Southeast of station Melpitz. Here and in the following maps the black dots represent  
 974 cities larger than 100000 inhabitants with the size of the dots being proportional to the  
 975 number of inhabitants.

976

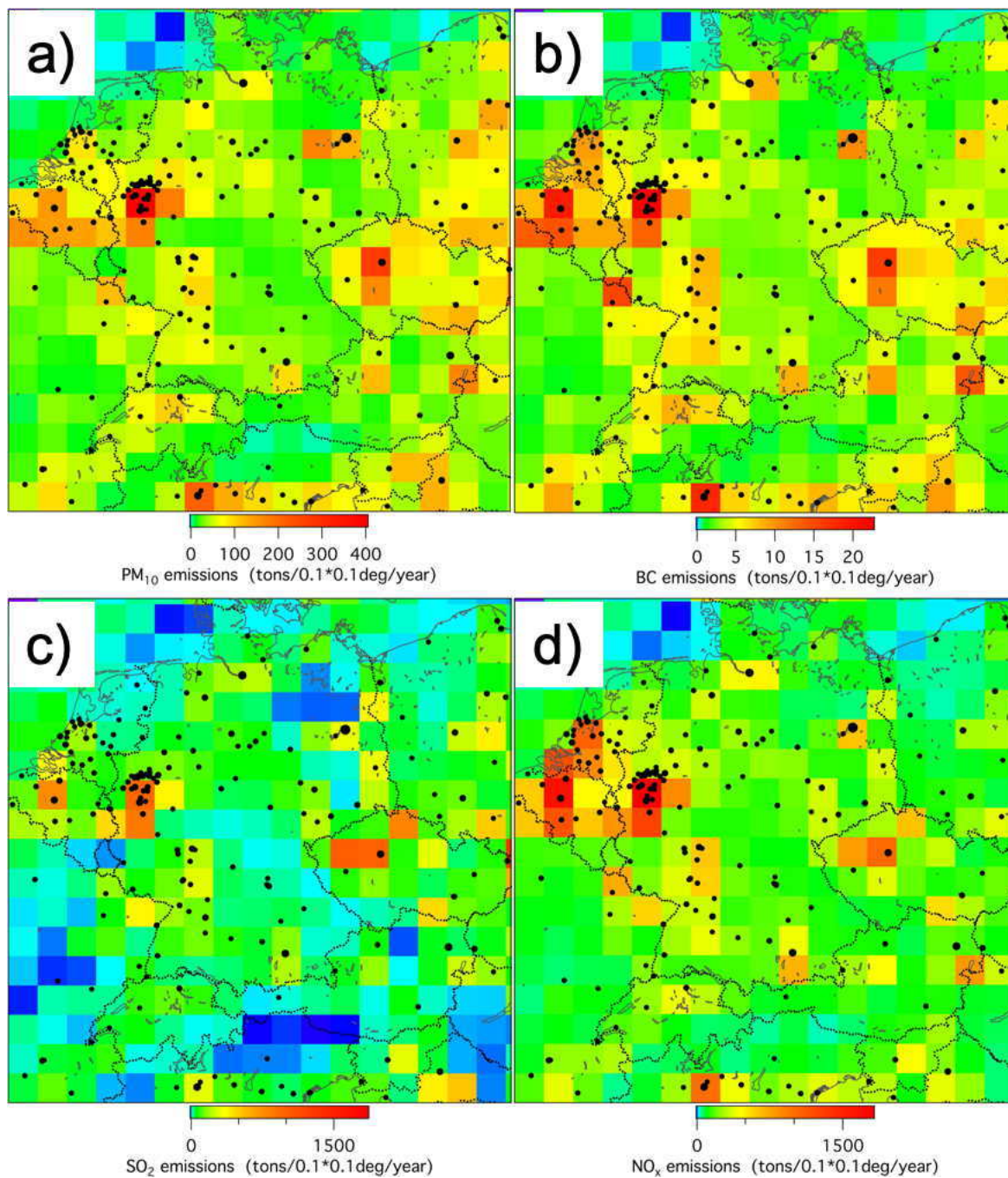


977

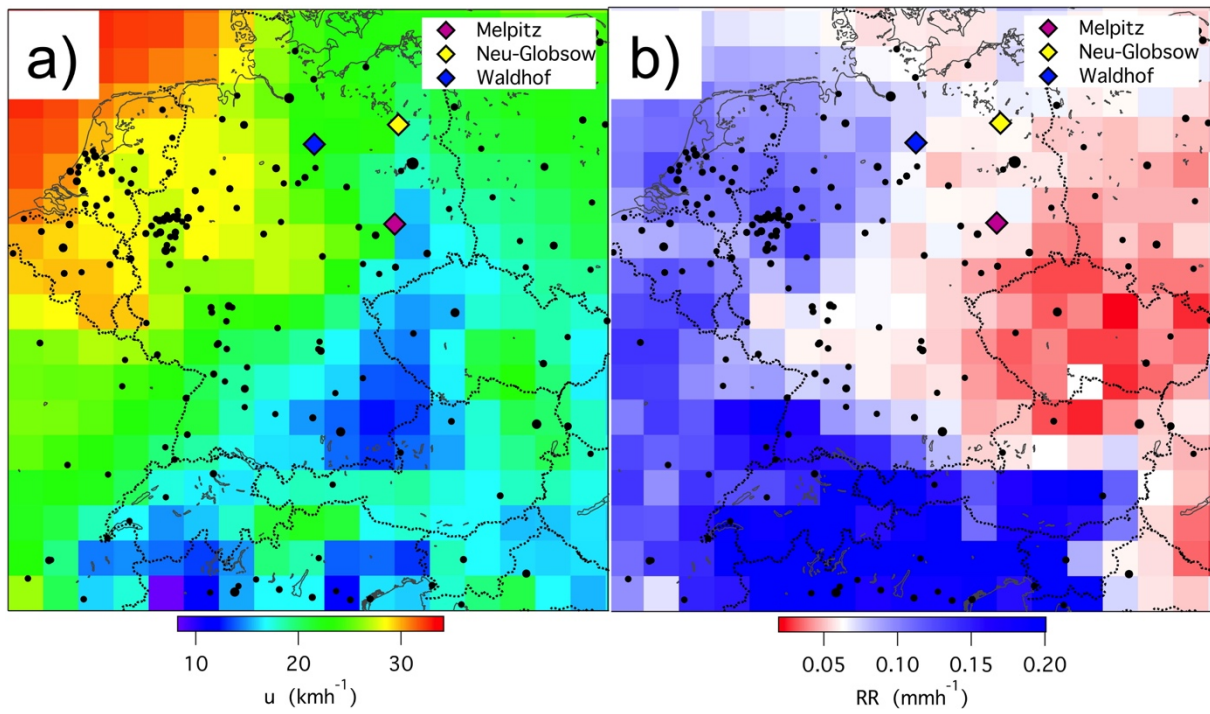
978 Fig. 2 As Fig. 1 but for particle mass concentrations (top, PM<sub>10</sub>, μgm<sup>-3</sup>), and black carbon

979 concentrations (bottom, eBC, μgm<sup>-3</sup>).

980



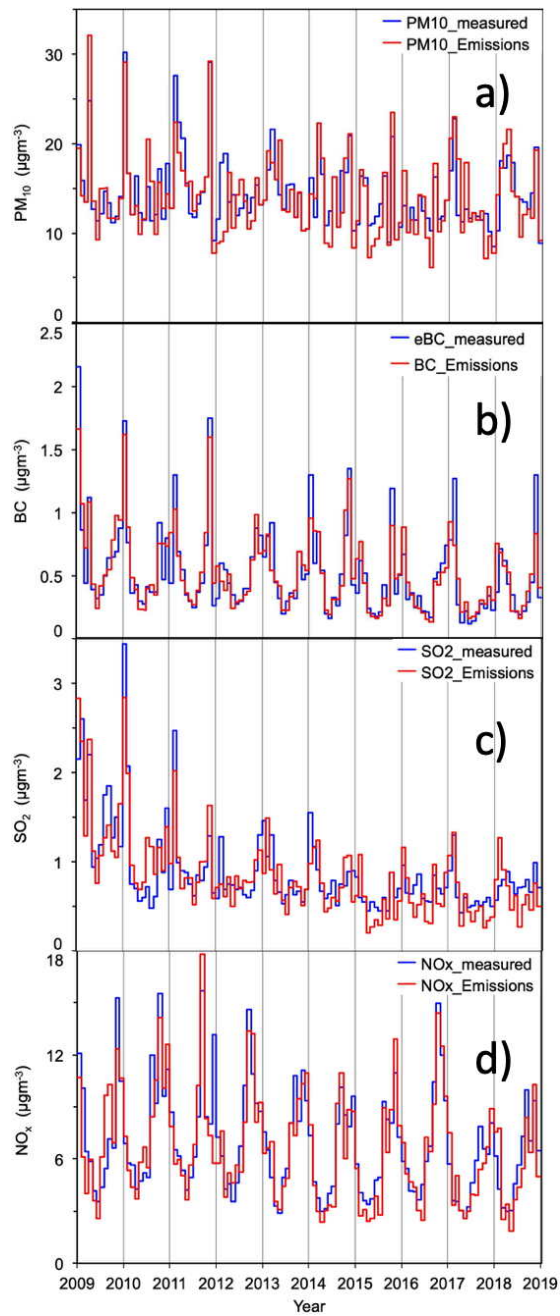
981  
 982 Fig. 3 As Fig. 1 but a) for PM<sub>10</sub> emissions (tons/0.1\*0.1deg./year), b) for BC emissions, c) for  
 983 SO<sub>2</sub> emissions, and d) for NO<sub>x</sub> emissions (tons/0.1\*0.1deg./year) according to the  
 984 EDGAR emission database  
 985 ([https://data.europa.eu/doi/10.2904/JRC\\_DATASET\\_EDGAR](https://data.europa.eu/doi/10.2904/JRC_DATASET_EDGAR)) for 2009 averaged over  
 986 the geogrid of the present study.  
 987



988

989 Fig. 4 a) Map of horizontal wind speed ( $u$ ,  $\text{kmh}^{-1}$ ) as reported by HYSPLIT along hourly five-  
 990 day back trajectories to the four stations marked in the graph averaged over the time  
 991 period 2009 to 2018; b) as a) but for precipitation ( $RR$ ,  $\text{mmh}^{-1}$ ).

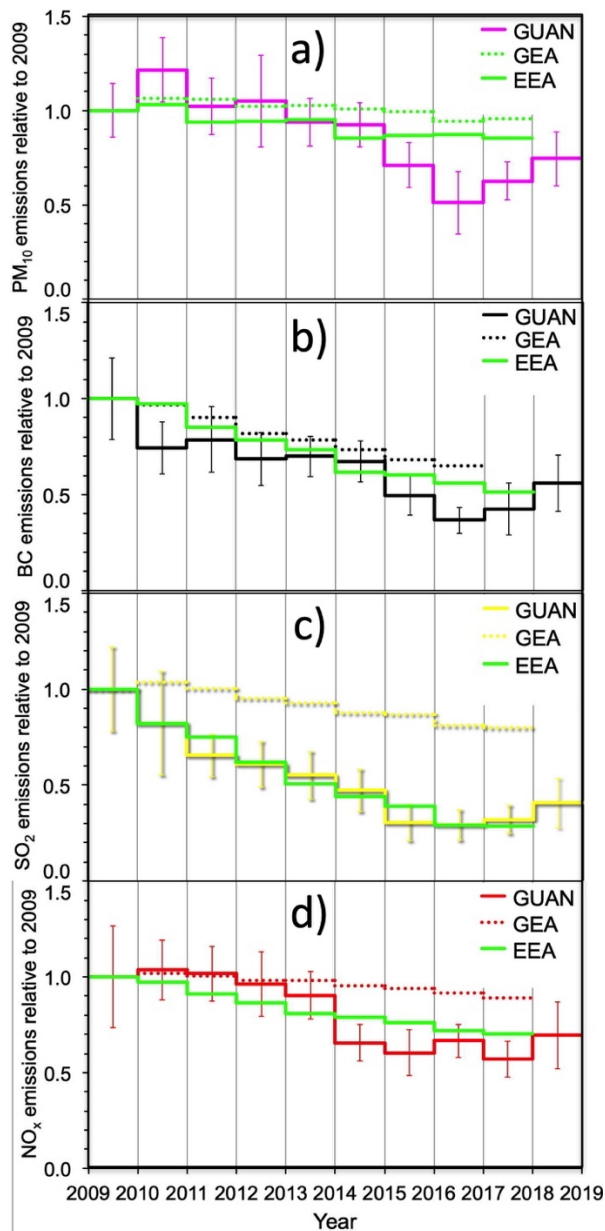
992



993

994 Fig. 5 a) Monthly medians of PM<sub>10</sub>-concentrations at the four stations of the present study  
 995 (blue), and monthly medians of optimized sums of PM<sub>10</sub>-emissions along back  
 996 trajectories leading to the stations (red). b) as a) but for measured eBC-concentrations  
 997 and BC-emissions along back trajectories. c) as a) but for measured SO<sub>2</sub>-concentrations  
 998 and SO<sub>2</sub>-emissions along back trajectories. d) as a) but for measured NO<sub>x</sub>-  
 999 concentrations and NO<sub>x</sub> -emissions along back trajectories.

1000



1001

1002 Fig. 6 GUAN: Trends in the emissions of a) PM<sub>10</sub>, b) BC, c) SO<sub>2</sub>, and d) NO<sub>x</sub>, relative to 2009

1003 as calculated by optimizing the agreement between 2009-EDGAR-emissions and

1004 concentrations measured at the four stations of the present study. The error bars

1005 represent annual average relative deviations between measured and simulated data.

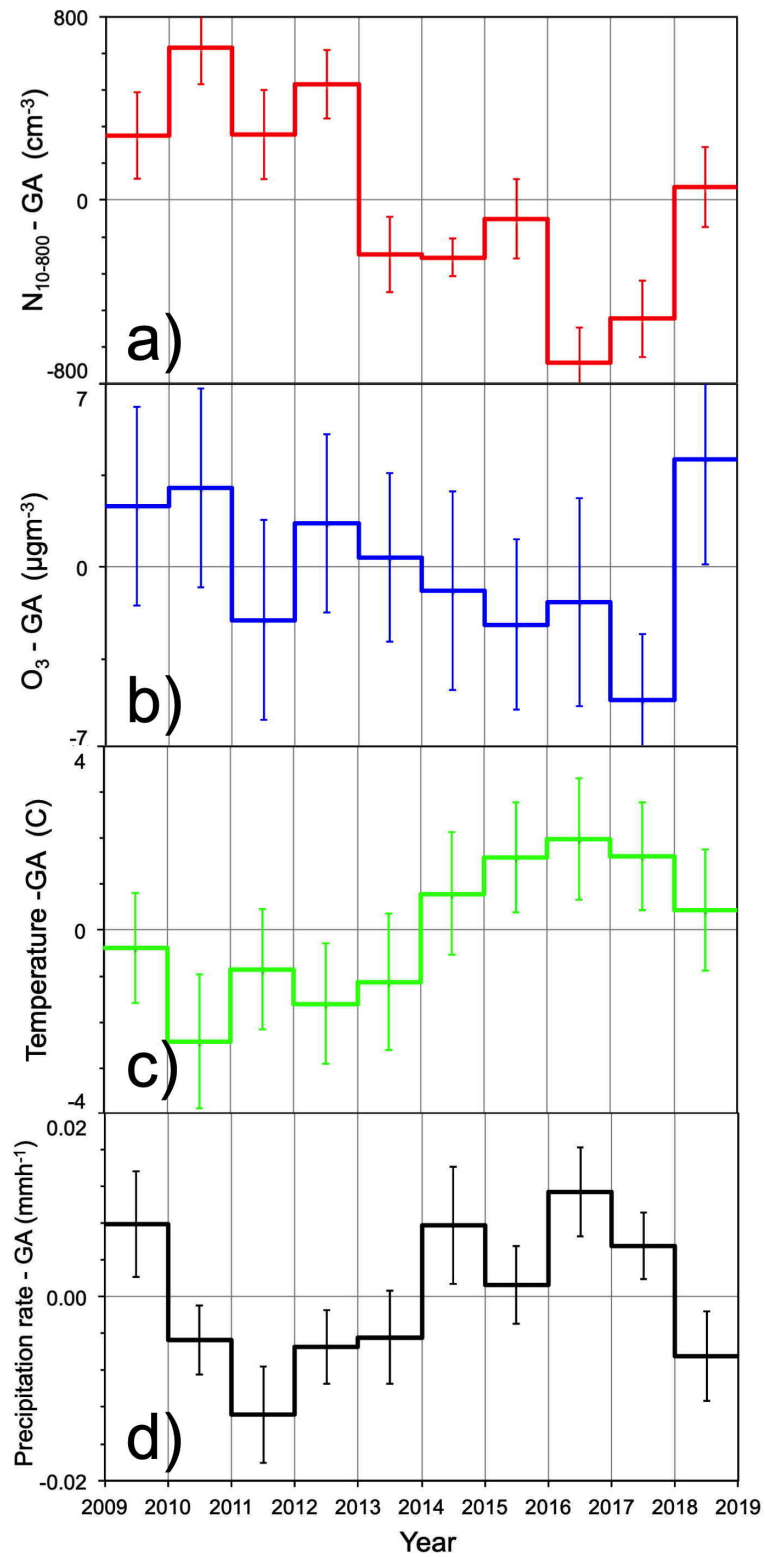
1006 GEA: Trends as reported for Germany by the German Environment Agency. EEA:

1007 Trends as optimized from combinations of trends over Germany and neighboring

1008 countries, (see text for details).

1009





1010

1011 Fig. 7 Trends in annual average deviations a)  $\Delta N_{10-800}$ , b)  $\Delta O_3$ , c) temperature  $\Delta T$  along the

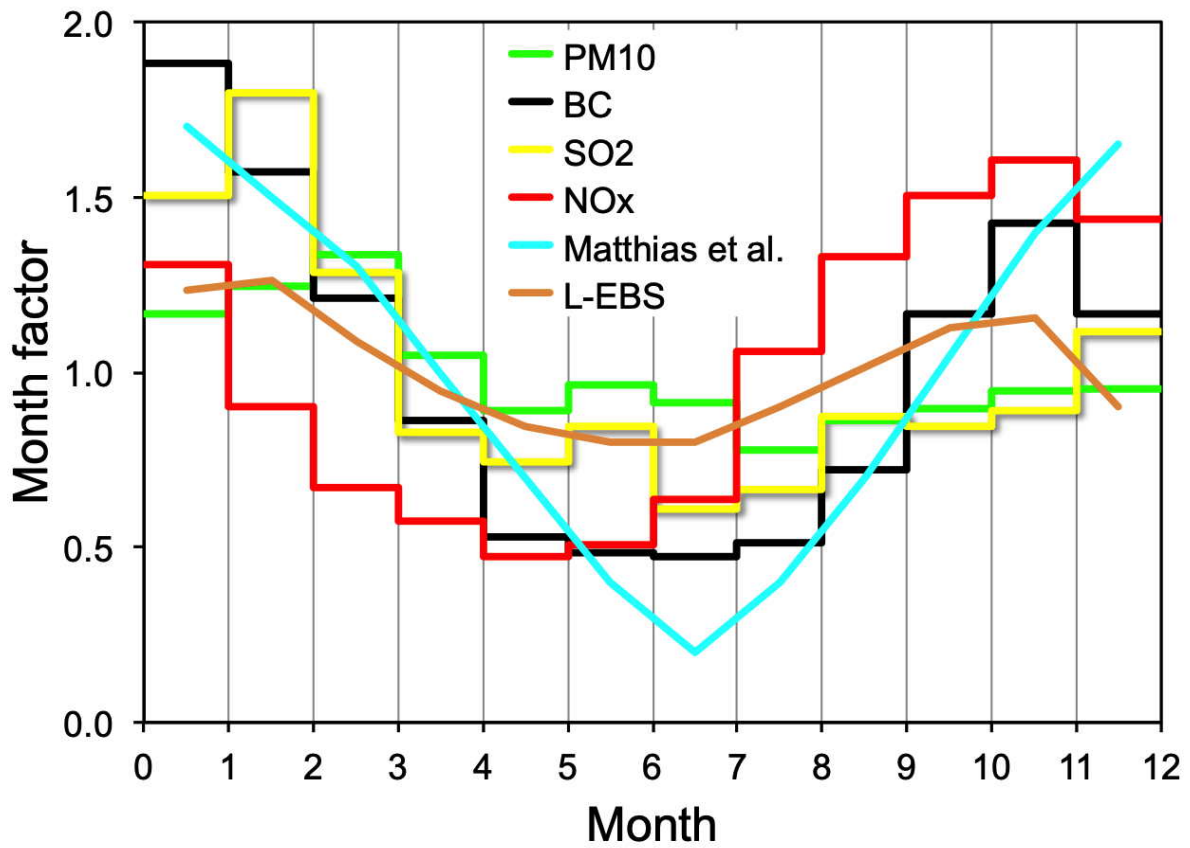
1012 trajectories five days back in time, and d) precipitation rate  $\Delta RR$  along the trajectories

1013 three days back in time. The deviations are taken relative to the respective 10-year

1014 Grand Average (GA). The error bars represent the standard deviations of the annual  
1015 averages.

1016

1017



1018

1019 Fig. 8 Month factors for the emissions of PM<sub>10</sub>, BC, SO<sub>2</sub>, and NO<sub>x</sub> as determined by  
1020 optimizing the agreement between EDGAR-emissions and concentrations measured at  
1021 the four stations of the present study. For comparison the month factors of Matthias et  
1022 al., (2018) for combustion emissions are plotted and the relative annual variation of eBC  
1023 concentrations measured at the station Leipzig-Eisenbahnstraße (L-EBS) averaged over  
1024 the time period of the present study.

1025

1026